

IV. AnAs. Actinide monoarsenides

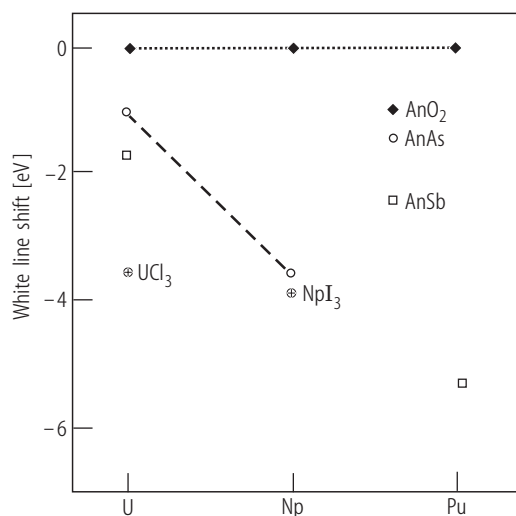


Fig. IV.1. AnAs, AnSb s.c. X-ray absorption white line shift of L_3 edge in monoarsenides and monoantimonides of U, Np and Pu compared to the respective dioxides [87KKBS1, 2]. Two observations are clear: 1) The increase in L_3 -edge shift for compounds with the same metalloid in direction from U to Pu, 2) as is the case of UAs and USb the shifts increase with increasing metalloid atomic number or decreasing with metalloid electron negativity.

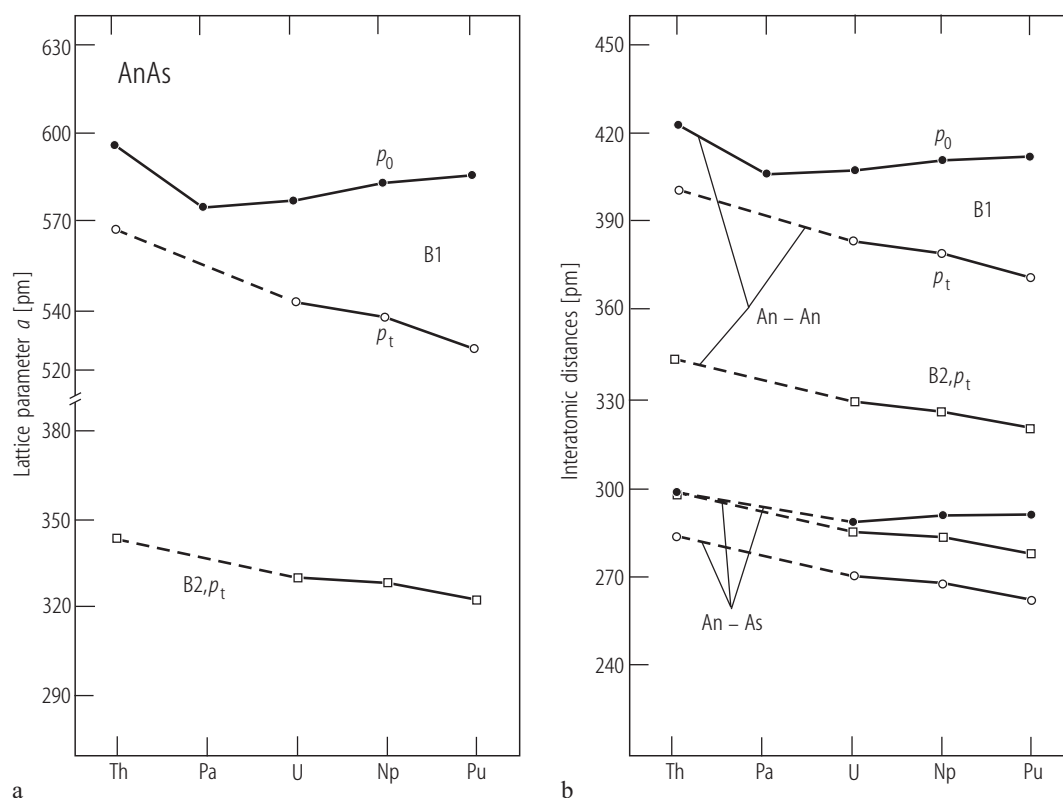


Fig. IV.2. AnAs (An = Th, Pa, U, Np, Pu). (a) Lattice parameter and (b) interatomic distances variations at ambient pressure p_0 and at the B1/B2 transition pressure p_t as a function of the actinide element [89DBSP]. Similarities are: all AnAs transform from NaCl-type to CsCl-type, ΔV collapse is $\sim 9\ldots 11\%$, there exists a strong hysteresis of the inverse transformation and an increase in

the An-As distance at p_t . Differences are: in values of the transition pressure p_t and in B_0 . No volume change occurs during the phase transition. The phase transition brings the ratio of the cation/anion radius outside the stability limit of the NaCl-type (0.41...0.73). The phase transition is not related to the 5f electrons.

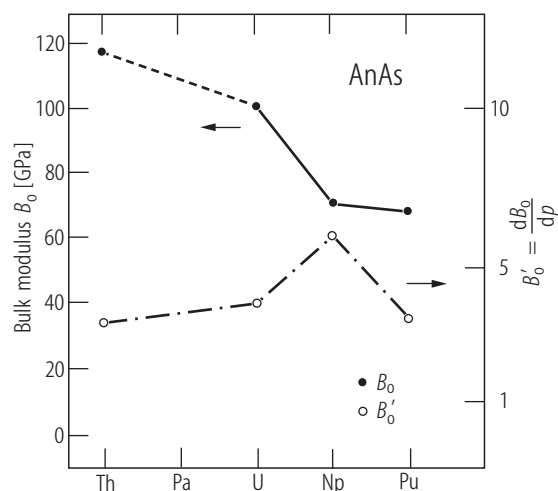


Fig. IV.3. AnAs. (An = Th, Pa, U, Np, Pu). Bulk moduli, B_0 (lhs), and its pressure derivatives, B'_0 (rhs), for the series of actinide monoarsenides as a function of the atomic number of the actinide element [89DBSP]. As seen, there is a tendency to decreasing bulk moduli towards nearer actinide elements. For the values see Table 6.

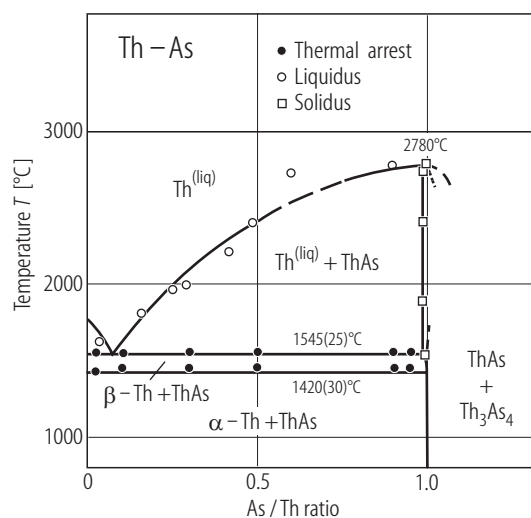


Fig. IV.4. ThAs. Thorium-ThAs phase diagram [68B]. The lattice parameter increases from $a_0 = 0.5973$ nm in the equilibrated products to $0.5976(1)$ nm in the annealed products (see also [55F]). For an As/Th ratio of 1.00 the congruent melting point is 2780 °C. The temperature of the eutectic is 1545(25)°C.

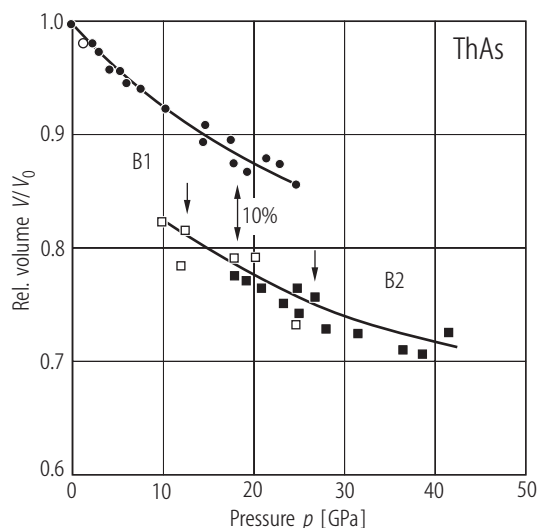


Fig. IV.5. ThAs. Relative volume V/V_0 vs. pressure, p , up to 43 GPa [88GSBD]. $a_0 = 0.6318(1)$ nm. The B1→B2 structure transformation takes place at 18 GPa, with a considerable hysteresis in the range of 9...26 GPa (see arrows). Full symbols: increasing pressure, open symbols: decreasing pressure.

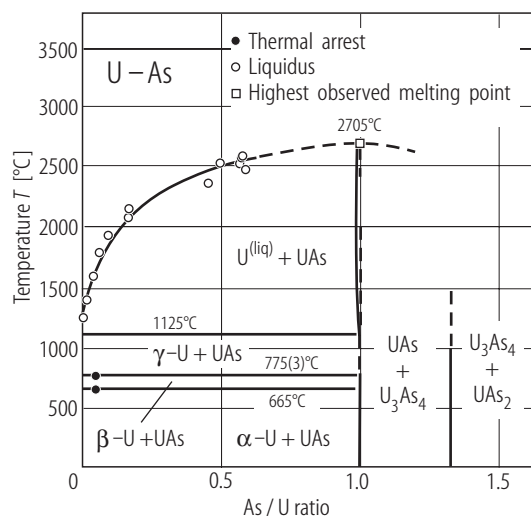


Fig. IV.7. UAs. Phase diagram U-As [68BT]. The U-UAs eutectic occurs at 1125(5)°C with a composition near pure uranium. Uranium solubility in UAs phase does not exceed 0.15%. $T_m = 2705$ °C, $a_0 = 0.57789(4)$ nm.

For Fig. IV.6 see next page

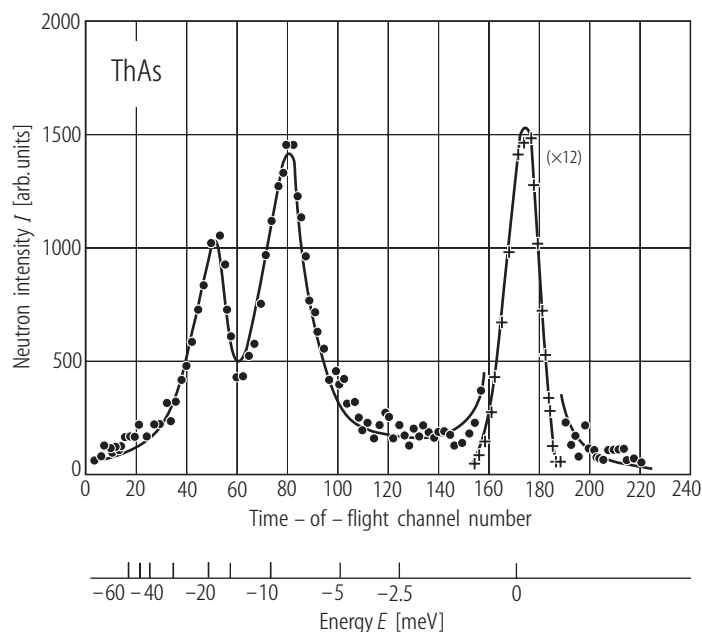


Fig. IV.6. ThAs. TOF scattering spectrum at RT ($Q = 0.92 \text{ \AA}^{-1}$) with incident neutrons of 3.62 meV [82LLMM]. The spectrum is composed of the incoherent nuclear elastic part at $\omega = 0$, the acoustic and phonon modes.

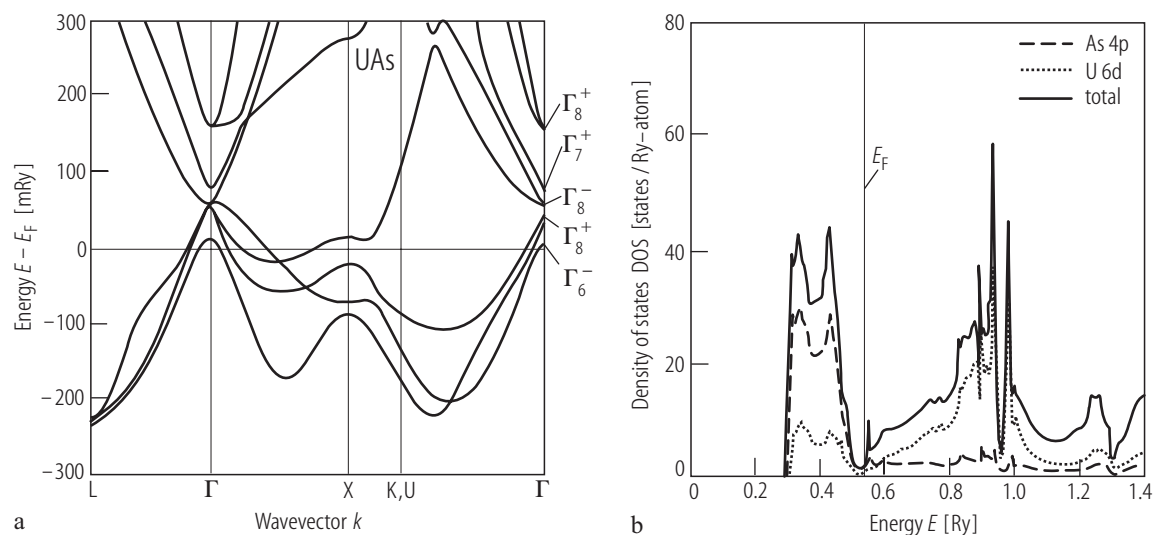


Fig. IV.8. UAs. (a) The band structure along symmetry lines in BZ based on the LMTO method and calculated with the U 5f states treated as core states [93KYCS]. Anion p-derived bands have Γ_6^- or Γ_8^- symmetry, while U 6d-derived

bands have Γ_7^+ and Γ_8^+ symmetry. (b) Total DOS (solid curves) derived from the band structure [93KYCS]. There are also the partial DOS for U d- (dotted curve) and As p- (dashed curve) derived bands.

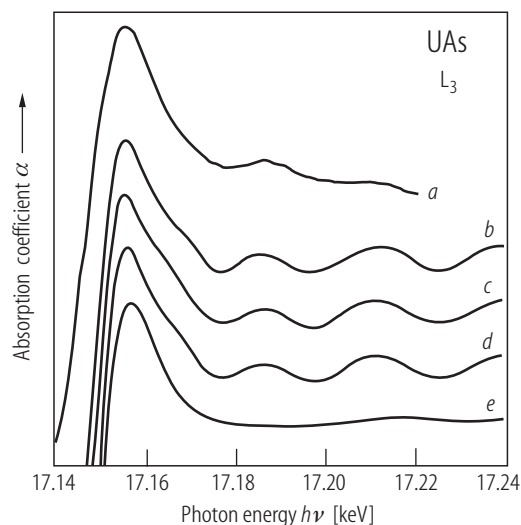


Fig. IV.9. UAs. FEFF-calculated L_3 -XANES for different types of scattering paths (curves *b-e*) [95HRB], compared to the experimental results taken from [87KKBS2], but shifted by 20 eV. Meanings: (*a*) experimental results, (*b*) MS with five shells, (*c*) SS with five shells, (*d*) SS with two shells and (*e*) SS with one shell, where SS is single scattering and MS is multiple scattering. Note that the calculation is nearly converged with only two coordination shells and single scattering.

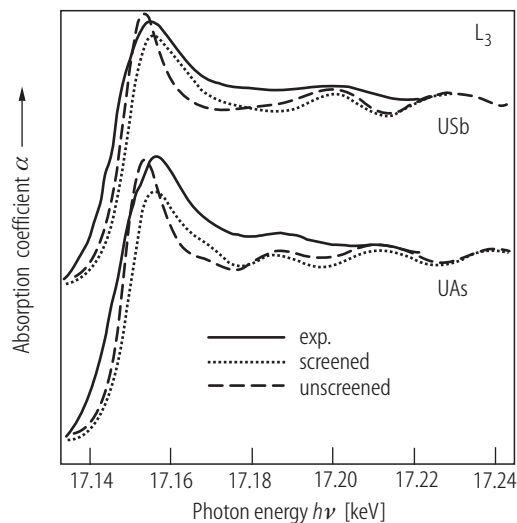


Fig. IV.10. UAs, USb. Comparison of experimental [87KKBS1] and FEFF-calculated [95HRB] uranium L_3 -edge XANES in UAs and USb. Calculations consist of results for a screened and unscreened core hole in the final state. Note a better agreement is with the screened state.

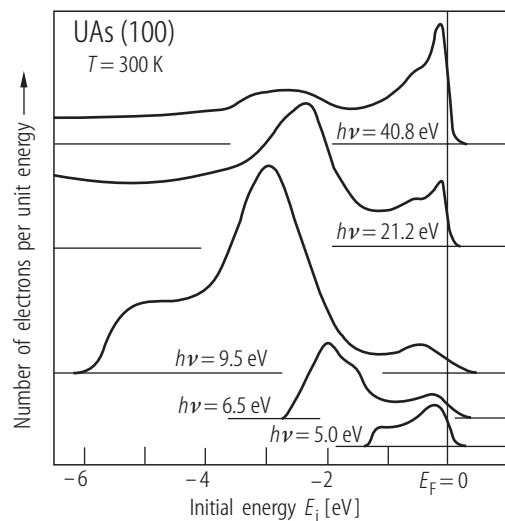


Fig. IV.11. UAs s.c. Energy distribution curves (EDC) as a function of initial energy, E_i , taken at various photon energies $h\nu$ for the (100) face [80GHOG]. These non-normalized spectra show a 1.5 eV wide 5f-6d band located near E_F and p derived band centered at -2.8 eV below E_F with a width of 2.5 eV. Note a structure in the f-d emission at -0.5 eV in the 21.2 eV and 40.8 eV spectra. This is not observed for the XPS spectra (see Fig. IV.12).

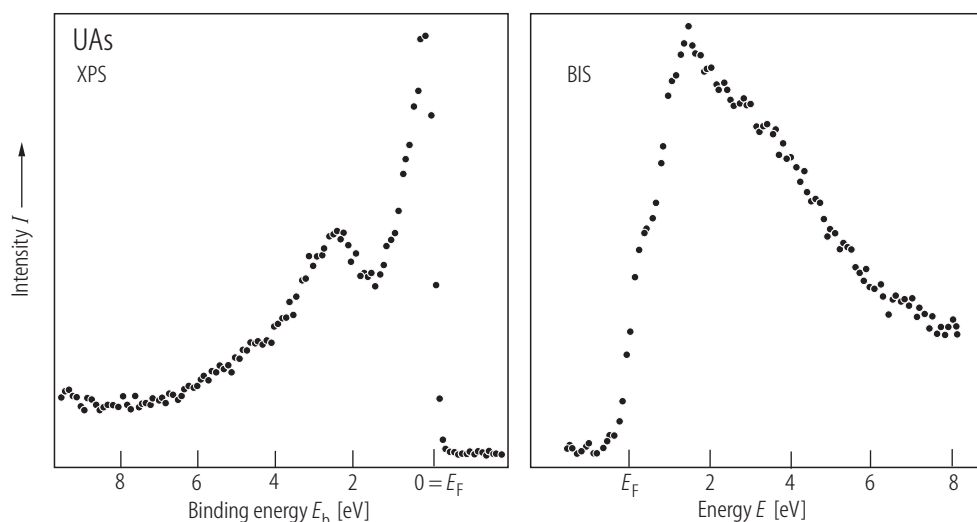


Fig. IV.12. UAs. XPS and BIS spectra [80B]. Note that except for the f-d band, which is cut by E_F , there is a distinct p band at 2.5 eV with the three weak structures predicted also by LMTO calculation of the DOS [80BG1]. The presence of two main peaks at 2 eV and 3.5 eV at the BIS spectrum is a general feature of 5f bands.

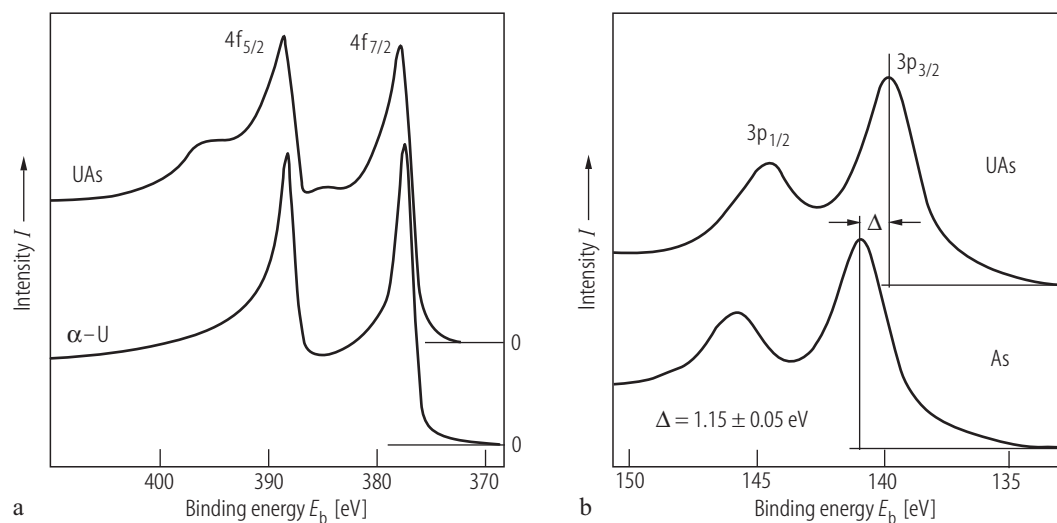


Fig. IV.13. UAs s.c. Electron core levels. **(a)** Uranium 4f core levels in UAs and α -U (not normalized) [80GHOG]. There is only a small shift (≈ 0.2 eV) in passing from α -U to UAs, but a larger broadening of FWHM from 2.4 eV to 5.8 eV and a strong increase of the 4f asymmetry. This is caused by a high DOS above E_F and multiplet splitting.

Note a core level satellite at 7.8(3) eV below the main lines, which is not observed in α -U. **(b)** Arsenic 3p core levels show a shift of $\Delta = 1.15(5)$ eV with respect to As and they are highly symmetric. This gives evidence of an appreciable charge transfer from U to As (about 1 electron) [80GHOG].

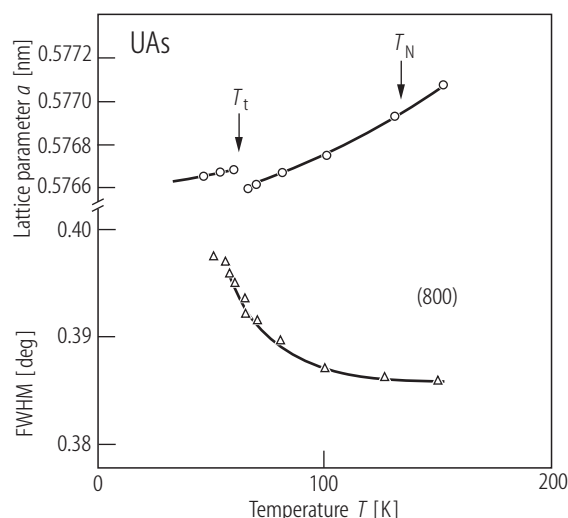


Fig. IV.14. UAs s.c. Lattice parameter a and FWHM for the (800) reflection measured with CuK_α radiation as a function of temperature down to 60 K [80KLMV]. No measurable distortions occur in the antiferromagnetic material in a limit of $|c/a - 1| < 2 \cdot 10^{-4}$ ($= \delta$). The increase in FWHM below T_N ($= 126$ K) which corresponds to $\delta = 1.5 \cdot 10^{-4}$ eventually may be connected with a tetragonal distortion. Note a small jump at $a = f(T)$ at T_t . Compare these results with those reported in [90MVII].

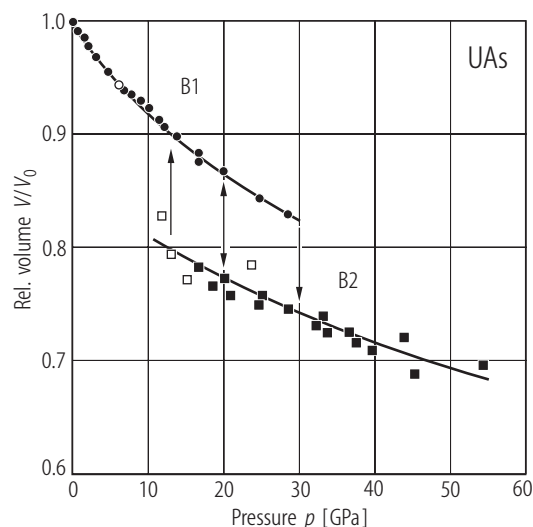


Fig. IV.16. UAs. Relative volume, V/V_0 , vs. pressure, p , up to 55 GPa [89SGBD]. B1: fcc NaCl-type structure, B2: primitive cubic CsCl-type structure. Full symbols: increasing pressure, open symbols: decreasing pressure. The solid curves were calculated from the equation of state. The B1-B2 phase transition extends over a considerable pressure range up to 30 GPa (p increases) and down to 12 GPa (p decreases). At 20 GPa a 11% volume collapse (double-sided arrow) ($a_0 = 0.57767(5)$ nm) takes place. The bulk modulus and its pressure derivatives are based on the Murnaghan equation (see [86SBGI]) and are given in Table 6 (see also Fig. R.25). Compare these results with those given for UAs up to 25 GPa in [88LVRR].

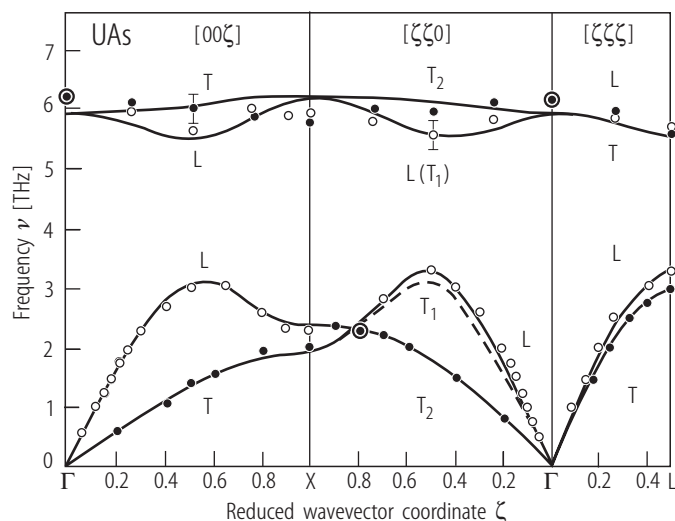


Fig. IV.15. UAs s.c. Phonon dispersion curves (PDC) [80SLV], [83SLV]. Open and closed circles are longitudinal (L) and transverse (T) modes, respectively. Solid curves are the best fits to simple lattice dynamical models, based on the six parameters (U-X, X-X, U-U, for both radial and tangential forces-see Table 10) of the conventional Born-von Kármán model, identical to that used by [71SG] to describe the lattice vibrations in UC (see Fig. I.29). The dashed curves describe the predictions of the model (see the original paper). Note the near degeneracy of the [110] acoustic TA and LA modes ($v_{LA} > v_{TA}$) at the X point of the BZ. However, no splitting of the optical TO and LO modes at the zone center Γ occurs. From the initial slopes of the acoustic phonon branches the following elastic constants for UAs were found: $c_{11} = 2.50(10)$, $c_{44} = 0.26(5)$ and $c_{12} = 0.10(15)$ – (all in 10^{12} dyn cm^{-2}). On the basis of the very small c_{12} -value there is a temptation to treat the UX compounds as intermediate-valence materials. For the calculated PDC's using a three-body interaction rigid-model with seven parameters see [92JS]. However, the model reproduces only some features of the PDC's.

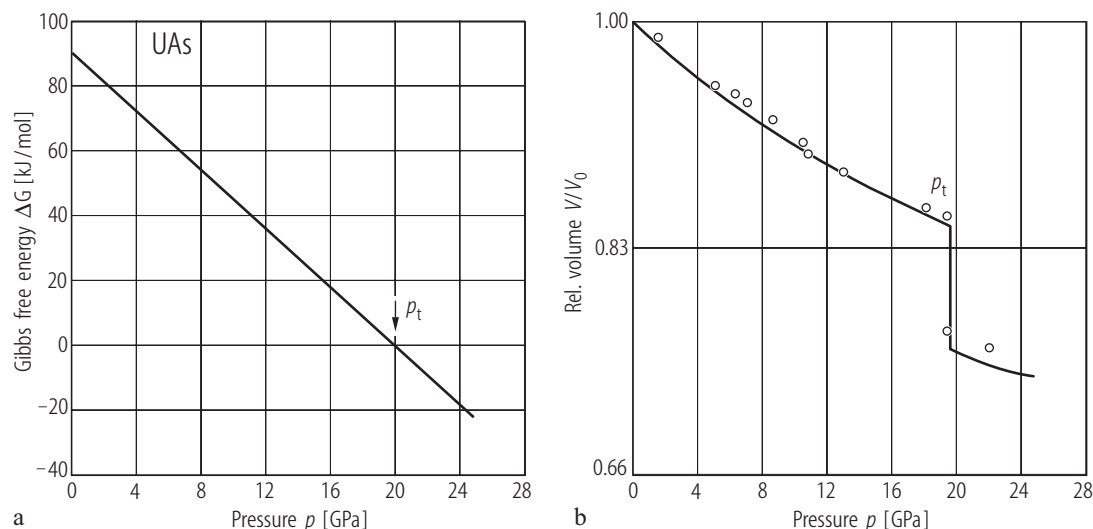


Fig. IV.17. UAs. (a) The difference in the Gibbs free energies ($\Delta G = G_{B1} - G_{B2}$) against the pressure, p , [97JS]. B1 and B2 are NaCl and CsCl structures, respectively. The transition between them is determined by the minima in the Gibbs energy. (b) Comparison between calculated and experimental results of $V/V_0 = f(p)$ taken from [88LVRR], [97JS]. In the calculation an interatomic potential $U(r)$

approach, based on rigid ion model formulation is used. This potential includes a long-range Coulomb, Hartree-Fock form of short-range repulsive energies and van der Waals multipole interactions (for the expression see the original paper). The calculated value of the phase transition pressure $p_t = 19.75$ GPa is close to the experimental value of 18.5 GPa [88LVRR].

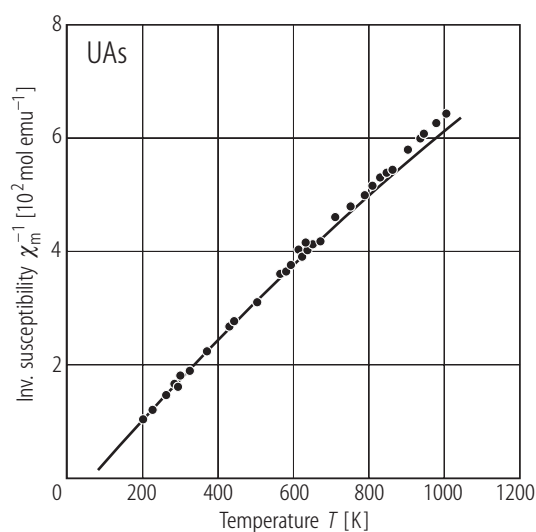


Fig. IV.18. UAs. Experimental inverse molar susceptibility, χ_m^{-1} , vs. temperature, T , measured up to 1000 K (closed circles) compared to the calculated susceptibility (solid curve) on the basis of a non-perturbative (full J -mixing) crystal field theory by assuming the $5f^3$ configuration and CEF parameters: $A_4\langle r^4 \rangle = 2000 \text{ cm}^{-1}$ and $A_6\langle r^6 \rangle \approx 0 \text{ cm}^{-1}$ [74TL].

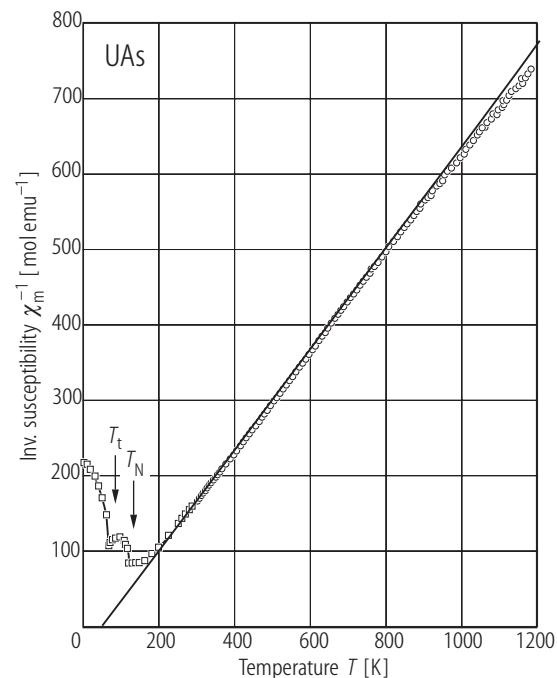


Fig. IV.19. UAs s.c. Inverse molar magnetic susceptibility, χ_m^{-1} , vs. temperature, T , measured up to 1180 K. The straight line represents the Curie-Weiss law. $\chi_m = \chi_{cw} + \chi_0$. A fit of a MCW law to the data gives $\Theta_p = 47 \text{ K}$, $p_{\text{eff}} = 3.43 \mu_B$ and $\chi_0 = 34 \cdot 10^{-6} \text{ emu/mol}$ [98VMLR].

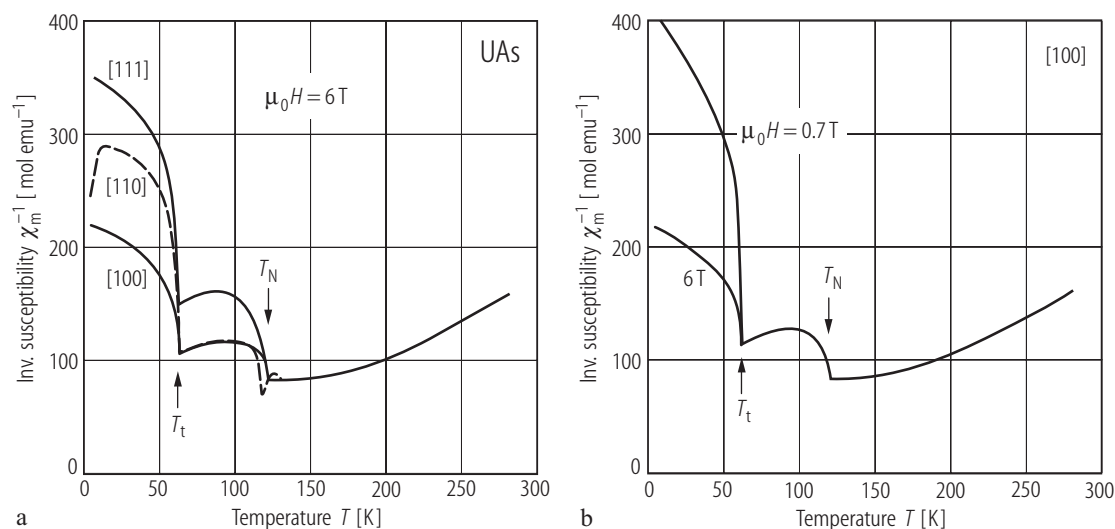


Fig. IV.20. UAs s.c. Inverse molar magnetic susceptibility, χ_m^{-1} , vs. temperature, T , measured (a) along three main axes [100], [110] and [111] in an applied field of 6 T, (b) along the [100] axis of a virgin crystal in two different applied fields of 0.7 and 6 T [78BV]. $T_N = 127$ K, $T_t = 66$ K.

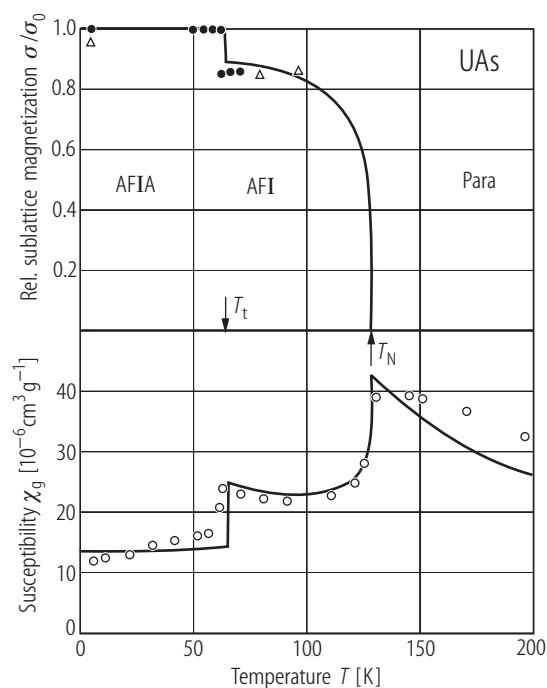


Fig. IV.21. UAs. Electron-delocalization model [73RE]: This model is assumed in the case of the overlap in energy of the localized 5f states and the itinerant-electron (6d-7s) band states. The free energy is analyzed in terms of the occupation numbers of the band and the magnetic sublevels of the localized states as shown in the case of UP (see the corresponding figures). This model is adapted also to UAs to yield the temperature dependence of the sublattice magnetization and band occupation. - Relative sublattice magnetization σ/σ_0 (upper panel) and specific powder susceptibility χ_g (lower panel) of UAs as a function of temperature T [74RE]. Experimental data are marked by the following symbols: closed circles [72LMR], open triangles [71LMP] and open circles [74TL]. $T_t = 63(2)$ K, $T_N = 127$ K. Solid lines present theory.

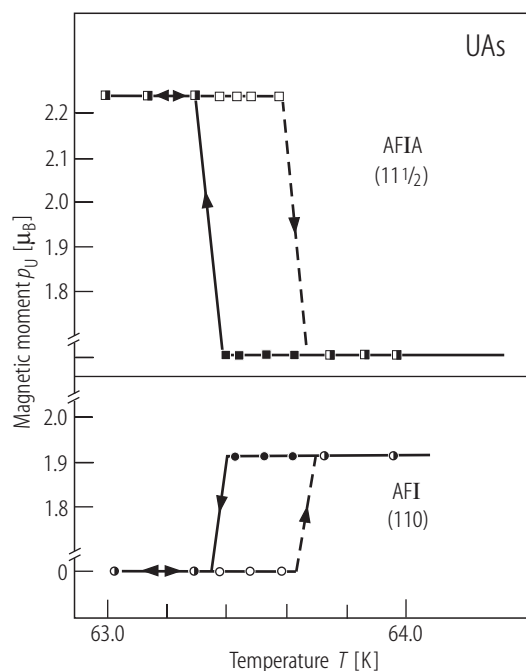


Fig. IV.22. UAs s.c. Magnetic moment, p_U , in AF IA- $2k$ ($1, 1, \frac{1}{2}$) and AF I- $1k$ (110), where it is equal to $2.20(5)\mu_B$ at 4.2 K and $1.93 \mu_B$ at 78 K (see Table 2), as a function of temperature around T_t ($= 63.5$ K) [81SLSV]. Closed points are obtained on cooling while open points on heating. Note a thermal hysteresis of 0.25 K which occurs at the T_t transition indicating that the IA-I transition is first order in accordance with the X-ray data [75MSWK] and [80KLMV]. The latter gave a proof of a volume discontinuity of $(V_{65K} - V_{5K})/V_{5K} = -4 \cdot 10^{-4}$ at T_t (see Fig. IV.14). Also any critical scattering was not observed at the transition T_t . For the first neutron diffraction studies on the polycrystalline samples see refs: [67TMZL], [68WHC], [68LKB] and [70LMPT].

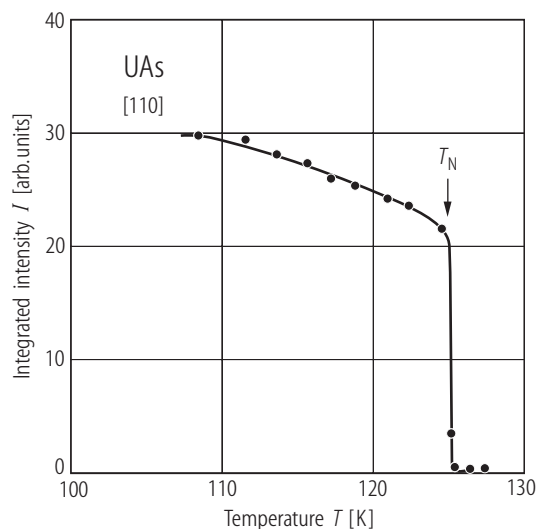


Fig. IV.23. UAs s.c. Neutron integrated intensity, I (variation of the magnetic Bragg peak (201)) in the vicinity of T_N ($= 123(1)$ K) for nearly single domain crystal [80RBBT]. The axial pressure is applied along the $[110]$ direction. The transition at T_N is mostly first order as that in UP (Fig. III.23a). The same results for a UAs single crystal are given in [81SLSV].

For Fig. IV.24 see next page

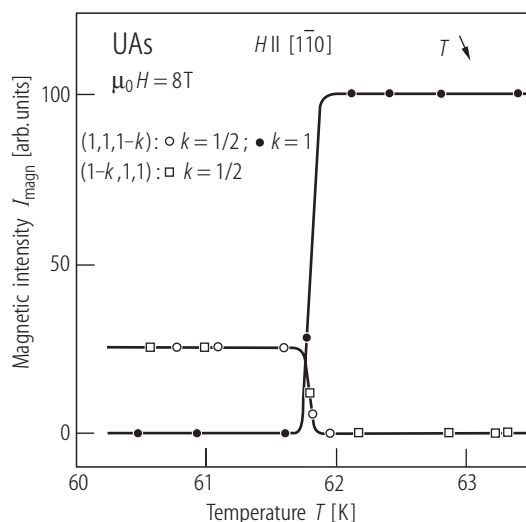


Fig. IV.25. UAs s.c. Intensity of magnetic peaks ($1, 1, \frac{1}{2}$) and ($\frac{1}{2}, 1, 1$) as a function of temperature around the type I – type IA transition T_t ($= 62$ K) in an applied field of 8 T [85RBQV]. Note the first-order transition from single- k to a double- k structure (compare it with Fig. III.23).

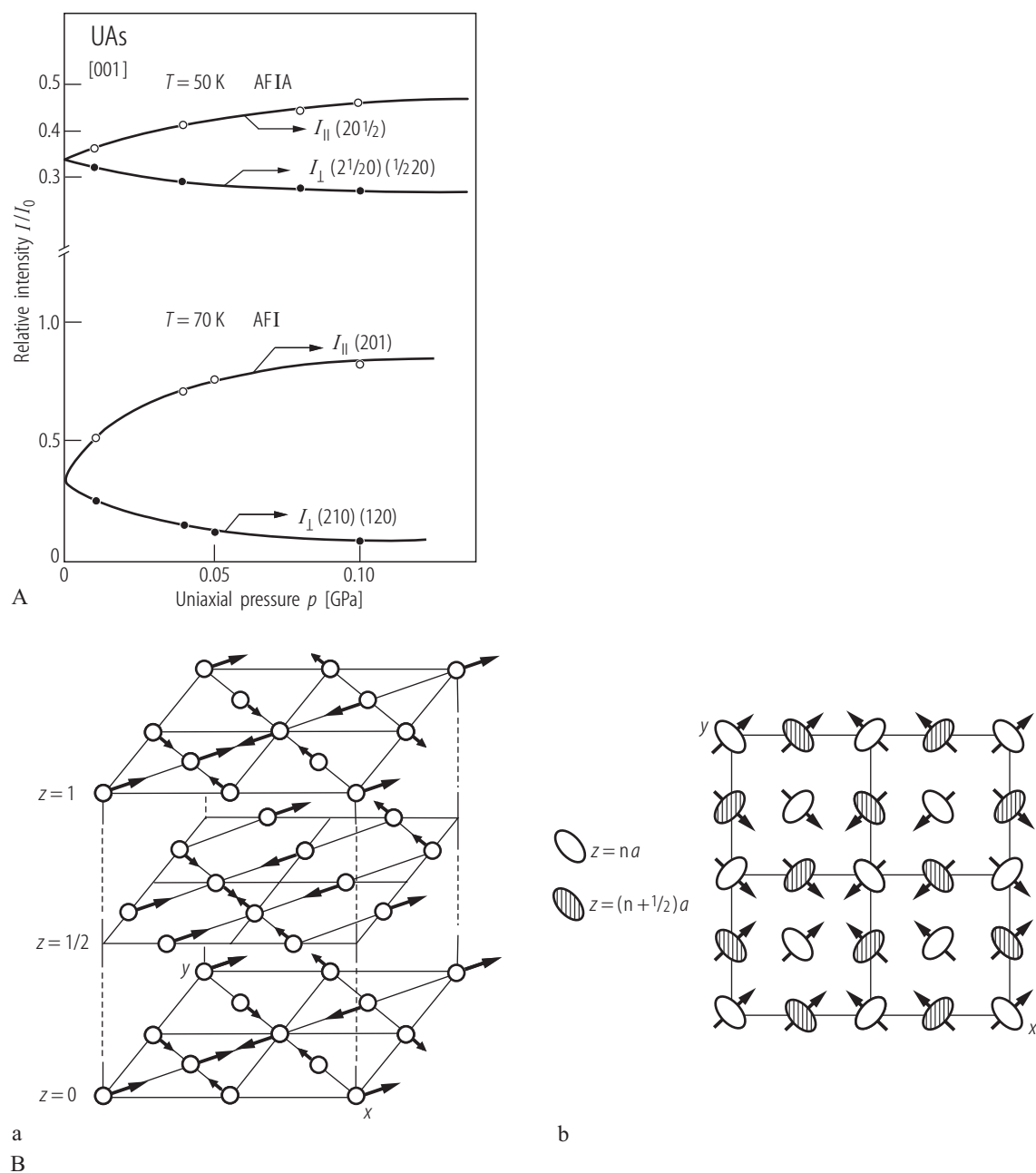


Fig. IV.24. UAs s.c. **(A)** The relative intensity, I/I_0 of the magnetic Bragg peaks (201) (AF I- $1\mathbf{k}$) and ($2\ 0\ \frac{1}{2}$) (AF IA- $2\mathbf{k}$) against a uniaxial pressure applied along the [001] direction [80RBBT]. These two Bragg peaks are associated to the three equivalent \mathbf{k} -vectors each. There are two domains having \mathbf{k} perpendicular to the stress which contribute equally to I_{\perp} , while the third one (\mathbf{k} parallel to the stress) gives an intensity I_{\parallel} . For saturation one gets $I_{\parallel} = 1$

and $I_{\perp} = 0$ if $c/a < 1$ in the case of AF I- $1\mathbf{k}$ and $I_{\parallel} = 0$ and $I_{\perp} = 1/2$ if $c/a > 1$. For the $2\mathbf{k}$ structure $I_{\parallel} = 0$ and $I_{\perp} = 1/2$ if $c/a < 1$ and $I_{\parallel} = 1/2$ and $I_{\perp} = 1/4$ if $c/a > 1$. The experiment predicts for $1\mathbf{k}$ $c/a < 1$ and for $2\mathbf{k}$ $c/a > 1$. **(B)** Magnetic structure of a type IA- $2\mathbf{k}$ determined by two wave vectors: $\mathbf{k}_1 = [\frac{1}{2}\ 0\ 0]$ and $\mathbf{k}_2 = [0\ \frac{1}{2}\ 0]$. **(a)** Three-dimensional magnetic unit cell **(b)** projection onto the (xy) plane.

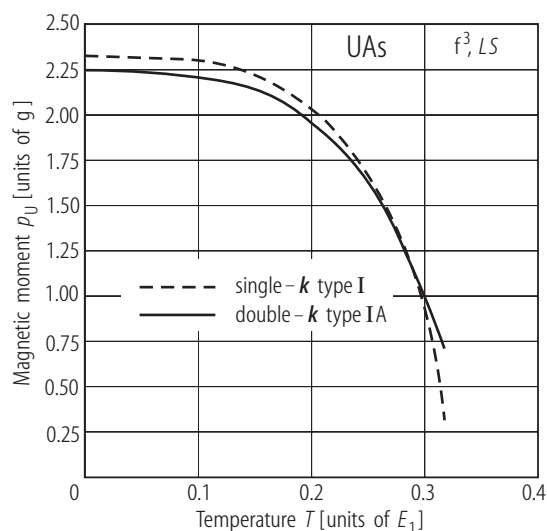


Fig. IV.26. UAs. Theory. Magnetic moment, p_U , vs. temperature, T (in units of E_1) for two magnetic structures: noncollinear AF IA-2 k (solid line) and collinear AF I-1 k (dashed line) [85TC]. The parameters calculated by the (HMI) model (for meaning see Fig. III.26 in the case of UP) are $E_1 = E_2 = 1$, $E_3 = -0.1$, $H_1 = -0.0392$, $W = -0.1$, $x = 1$. The free energies of these two structures are nearly equal to each other (not shown), only a small difference in p_U exists. The fourth-order CEF parameter V_4 obtained by matching to T_N ($= 125$ K) is close to that given in [74TL].

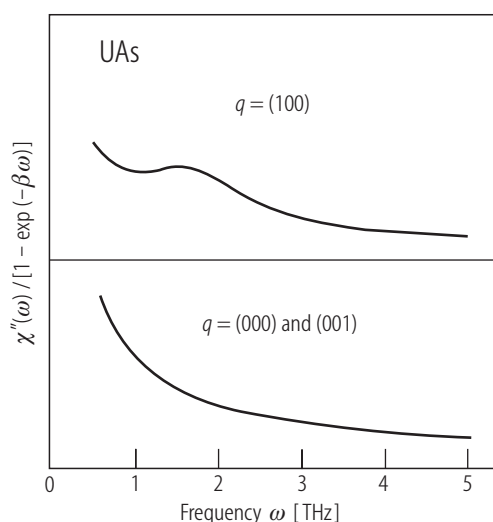


Fig. IV.27. UAs. Calculated imaginary part of the dynamic susceptibility, $\chi''(\omega)$, vs. frequency, ω , for the AF I-phase at 11 K at the zone center $q = (000)$ and zone boundaries (001) and (100) [88HC] and [93HC]. The following parameters were used: $E_2/E_1 = 1$, $E_3/E_1 = -0.5$, $W = 0.02E_1$, $x = 1$ ($E_1 = 500$ K, $T_N = 127$ K), $J N(E_F) = -0.12$. For some details see also the caption of Fig. III.27. The comparison between UP and UAs indicates that the two ion exchange interaction for the latter compound is considerably larger ($E_1 = 500$ K) than that for the former compound ($E_1 = 215.5$ K). However, this is much larger than for Ce^{3+} systems ($E_1 = 15.4$ K for CeSb and 19 K for CeBi). In general the calculation results are in agreement with those of inelastic neutron scattering experiments for UAs [80SLV] and [80LS].

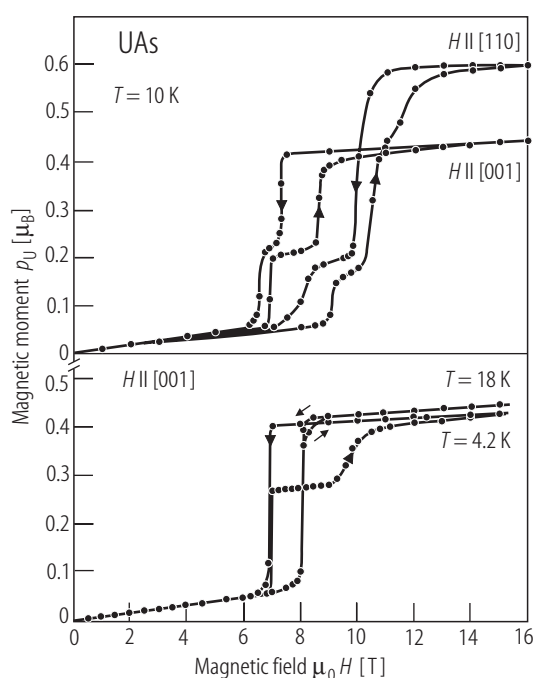


Fig. IV.28. UAs s.c. Magnetic moment, p_U vs. magnetic field, H , applied along $[001]$ and $[110]$ at 10 K (upper panel) and along $[001]$ at 4.2 K and 18 K (lower panel) [85RBQV]. For $H \parallel [110]$ the magnetization changes its values with increasing magnetic field strengths reaching finally a larger value than that in the case $H \parallel [001]$. This indicates the flipping of the first and then the second moment components of the AF IA-2 k structure. For $H \parallel [001]$ the transition is sharp at higher temperature (18 K) and gradual at 4.2 K.

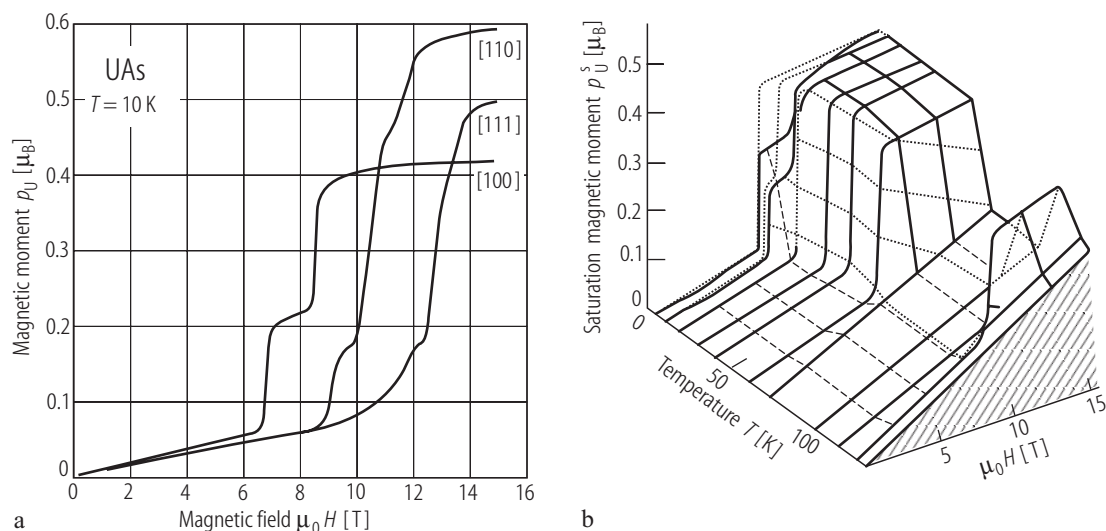


Fig. IV.29. UAs s.c. **(a)** Magnetic moment, p_U , vs. magnetic field, H , up to 15 T measured along three main axes at 10 K [79BVB]. Note the step behaviour due to the formation of intermediated magnetic structures (see MPD in Fig. IV.31). Saturation moment p_S (at 15 T) is equal to 0.44, 0.60 and 0.49 μ_B along the [100], [110] and [111] direction, respectively. Nevertheless, the states observed at 15 T have a much lower moment than the full one (2.20 μ_B), found in neutron diffraction [68LMT]. These values are in accordance with the $\cos\theta$ law, indicating strong uniaxial

anisotropy. However, the lowest threshold field H_{cr} is not along the easy axis [110] but along [100] according with the double \mathbf{k} -ferri structure. The threshold fields are essentially temperature independent. **(b)** Three dimensional (p_U^S, T, H) MPD along the [100] direction [79BVB]. Note that above 66 K H_{cr} cannot be observed due to too lower fields applied until temperatures are close to T_N (compare it with (T, H) MPD in Fig. IV.31). The dotted lines are guides for the eyes.

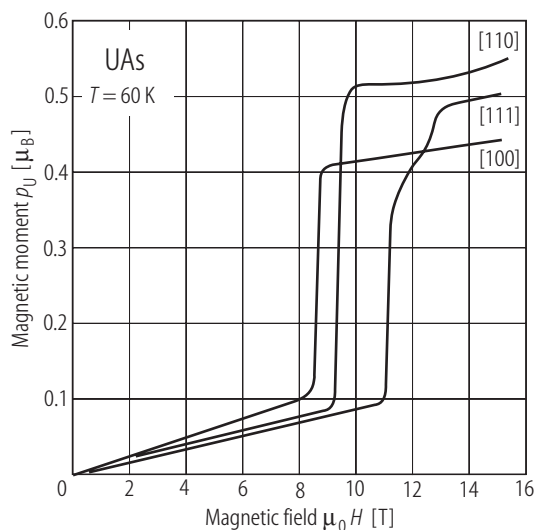


Fig. IV.30. UAs s.c. Magnetic moment, p_U , vs. magnetic field, H , applied along three principal axes up to 15 T at 60 K (i.e. within the AF IA-2 \mathbf{k} structure) [78BV]. Note the metamagnetic transitions to an intermediate ferromagnetic structure with a fraction (1/3) of the full moment. The threshold fields H_{cr} depend on the crystal axis and in contrast to UP it is lowest for $H \parallel [100]$. However, the easy axis is [110] as is the case of UP below $T = T_i$ (see Fig. III.28).

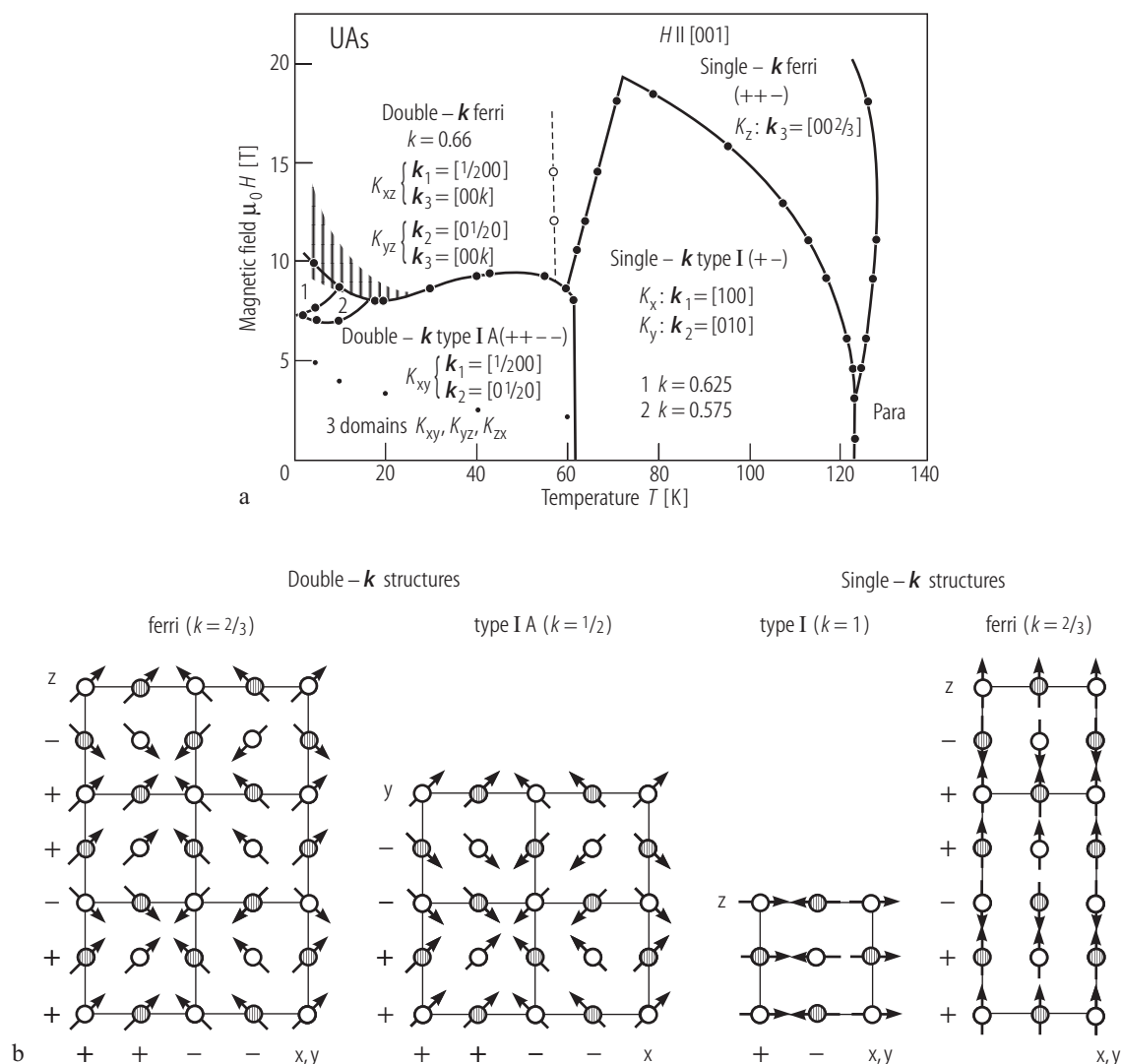


Fig. IV.31. UAs s.c. **(a)** (H,T) MPD for a magnetic field applied along the $[001]$ axis [82RBQV]. $T_N = 124.5(1)$ K at $H = 0$. The solid lines are transition lines obtained by scans at constant T at temperatures $T < T_i$ ($= 62$ K) and by scans at constant H for $T > T_i$. Note that besides the antiferromagnetic phases AFI- $1k$ and AF IA- $2k$ the magnetic field induces ferrimagnetic phases (indicated). The domain characteristics K_i and K_{ij} are also presented, respectively. Note a complex step-like character of transitions toward induced ferrimagnetic state at low temperatures (hatched area). For

$T < 62$ K a single domain K_{xy} associated with AF IA- $2k$ structure is obtained in fields 2.5...5 T (see small dots). The dashed line denotes a weak magnetization anomaly observed at $T \approx 55$ K and $H > 10$ T. **(b)** Projection of the following magnetic structures occurring in MPD of UAs: Ferri- $2k$, type IA- $2k$, type I- $1k$ and Ferri- $1k$ onto the $xz(y)$, yx , $zx(y)$ and xy planes, respectively [82RBQV]. Shaded symbols refer to projections of moments of the atoms located in the adjacent plane.

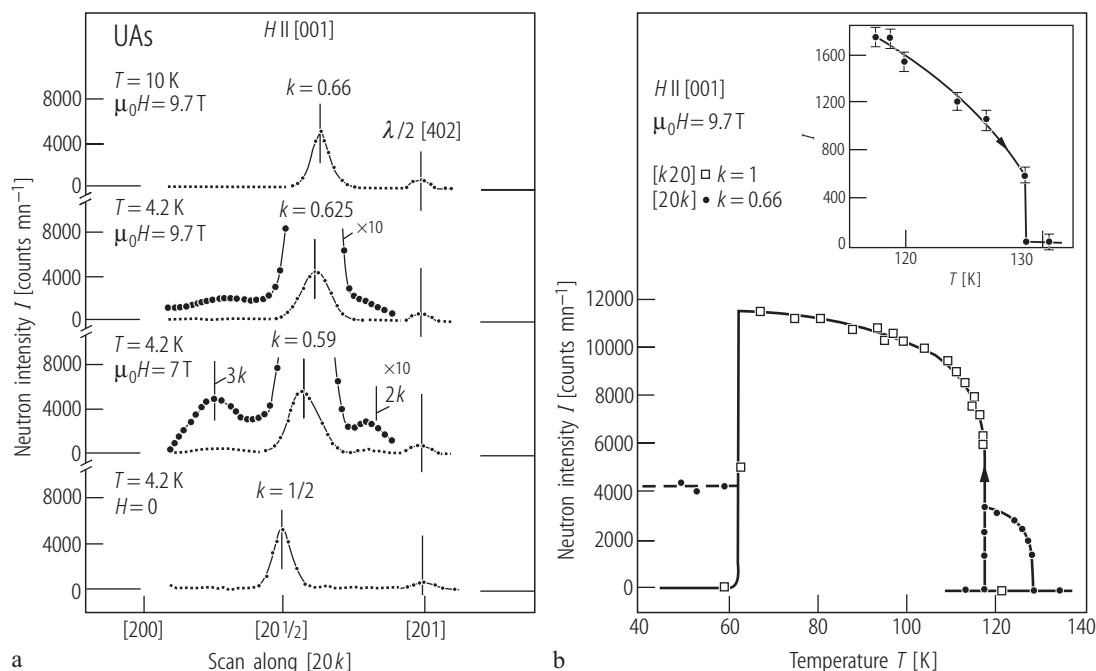


Fig. IV.32. UAs s.c. (a) Neutron intensity, I , of the scattering along the $[20k]$ direction for $H \parallel [001]$, measured at different temperatures T (4.2 and 10 K) and fields H (7 and 9.7 T) [82RBQV]. The scans indicate new superlattice peaks associated with a wave vector $k = [00k]$, where $k = 0.590(5)$ having its second ($2k = 0.82(1)$) and third ($3k = 0.27(1)$) harmonics. For comparison, the scan showing the structure with $k = 1/2$ (AF IA) found at 4.2 K and $H = 0$ is

presented in the bottom panel. For the range of existence of the above structures in MPD of UAs see Fig. IV.31. See also high-field neutron diffraction data of [79FLDV]. (b) Neutron intensity, I vs. temperature, T , of superlattice peaks (indicated), measured at 9.7 T for $H \parallel [001]$ [82RBQV]. As seen, the transitions from the AF I phase to the ferrimagnetic one and then to the paramagnetic phase are both first order.

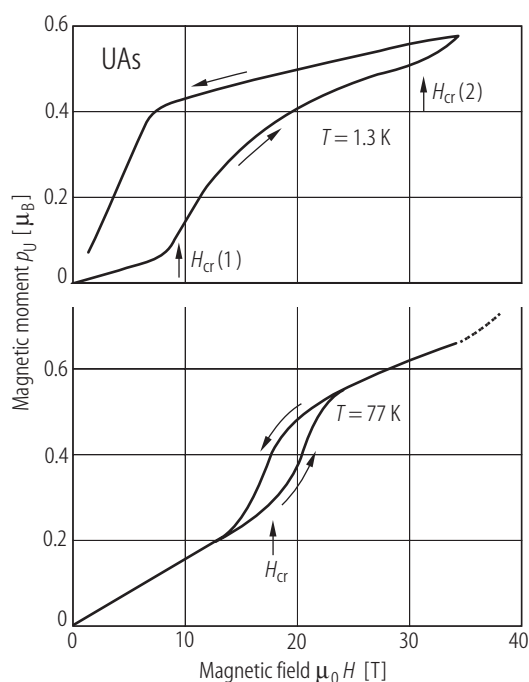


Fig. IV.33. UAs. Magnetic moment, p_U , vs. applied magnetic fields up to 38 T for a polycrystalline sample at two temperatures as indicated [78ST]. Note two values of critical field $\mu_0 H_{cr}(1) \approx 9.5 \text{ T}$ and $\mu_0 H_{cr}(2) \approx 30 \text{ T}$ determined at 1.3 K. The first critical field is in accordance with single crystalline data presented in Fig. IV.31. The saturation moment $p_S \approx 0.6 \mu_B$ at 1.3 K being close to one third of the full value $2.2 \mu_B$ [68LMT]. Also in accordance with single-crystalline data, at 77 K, there is only one clear transition at about 20 T and in addition a slight indication of a second one at the highest applied fields of 38 T.

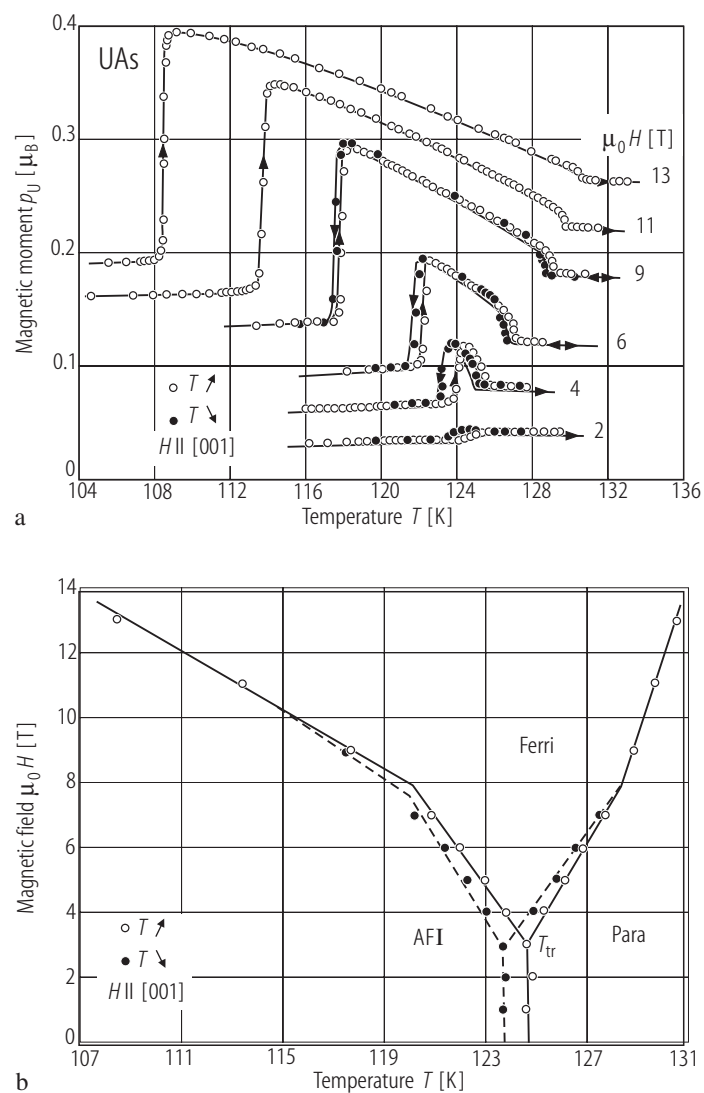


Fig. IV.34. UAs. s.c. **(a)** Magnetic moment p_U , vs. temperature, T , around T_N in magnetic fields of 2...13 T applied along the [001] axis [80RBBT]. The first-order transition is well illustrated by a sharp jump in p_U . Note that the hysteresis being about 1 K in low fields decreases as the magnetic field increases. **(b)** (H, T) MPD determined around T_N [80RBBT]. See the triple point at $T_{tr} = 124.4$ K and $\mu_0 H_{tp} = 3$ T where the “ferri- AF I” and paramagnetic phases coexist.

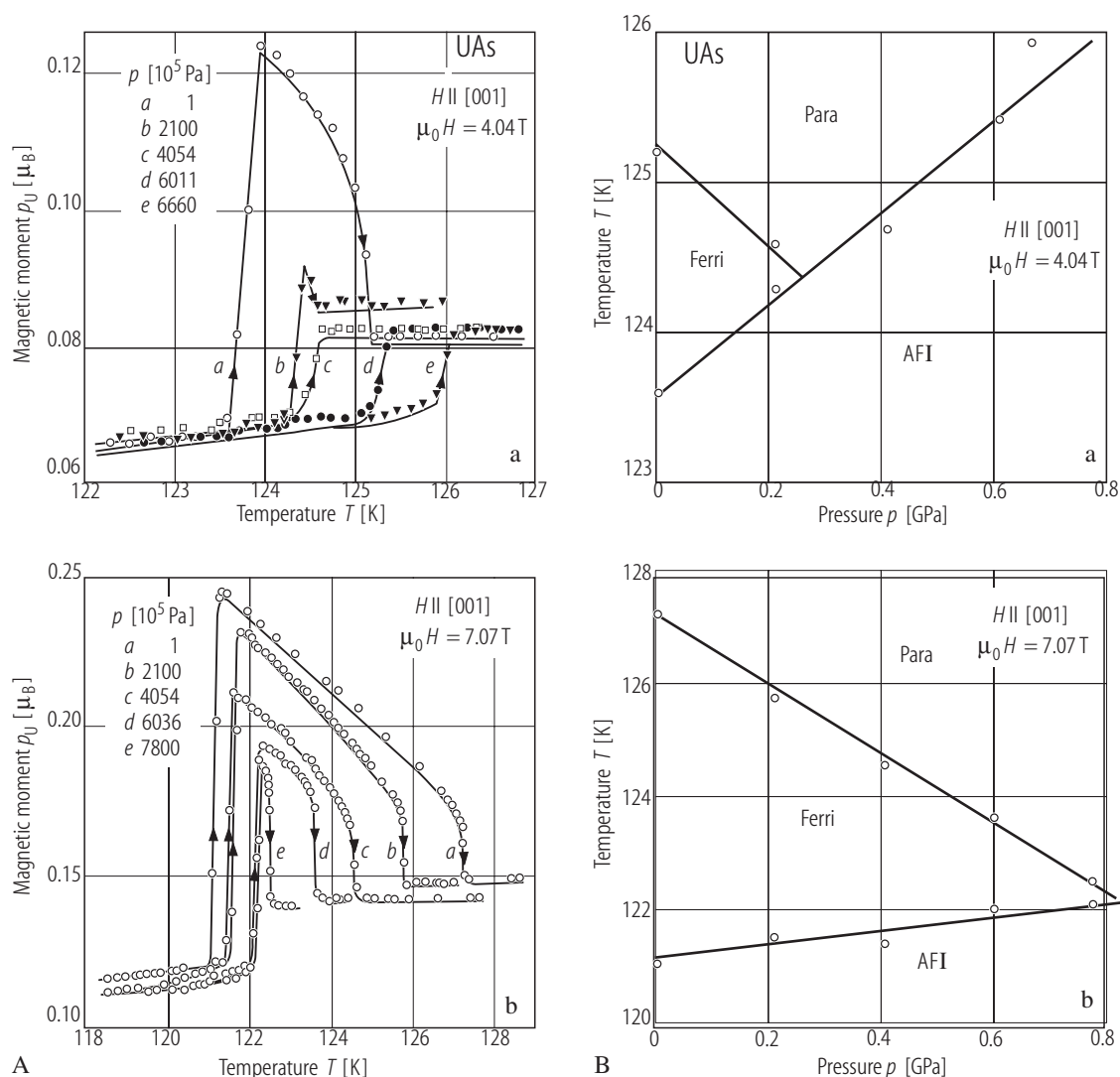


Fig. IV.35. UAs s.c. **(A)** Magnetic moment μ_0 , vs. temperature, T , in the vicinity of the T_N measured in two different magnetic fields: **(a)** 4.04 T and **(b)** 7.07 T applied along the [001] axis and under several pressures up to 0.8 GPa (indicated) [80RBBT]. **(B)** (T, p) MPD determined in two applied magnetic fields: **(a)** 4.04 T and **(b)** 7.07 T [80RBBT]. The induced “ferrimagnetic” state disappears at

0.25 and 0.85 GPa, respectively. Note opposite changes in the temperatures of transitions AF I-Ferri or AF I-Para compared to Ferri-Para and a shift of the stability range of the Ferri-phase to higher field and lower temperatures. As $dT_N/dp > 0$, a decrease in the volume occurs at T_N and a tetragonal distortion is $c/a < 1$ in accordance with the uniaxial stress results (Fig. IV.24A).

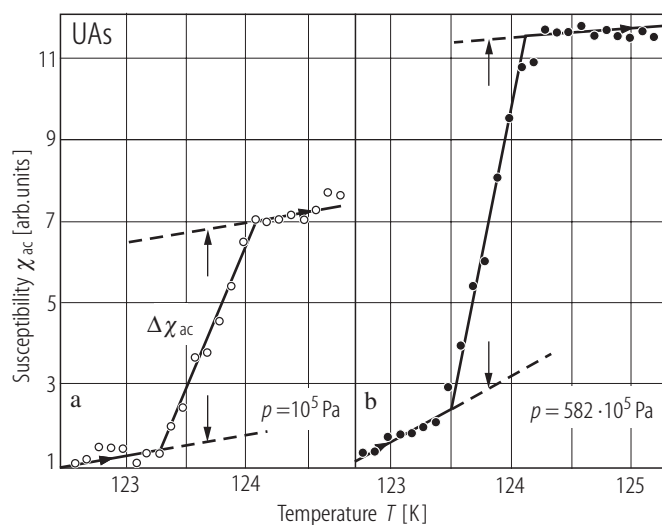


Fig. IV.36. UAs s.c. ac magnetic susceptibility, χ_{ac} , (in arb. units) vs. temperature around T_N (a) without and (b) with a uniaxial stress applied along the [001] axis [80RBBT]. The discontinuity $\Delta\chi_{ac}$ ($= 2 \cdot 10^{-3}$ emu/mol) at T_N , being in accordance with [74TL] is due to a first-order transition (figure (a)). Note that this susceptibility jump increases with the uniaxial stress (figure (b)), which in saturation at about $582 \cdot 10^5$ Pa becomes 1.5 times larger than that at 10^5 Pa ($= 1$ bar).

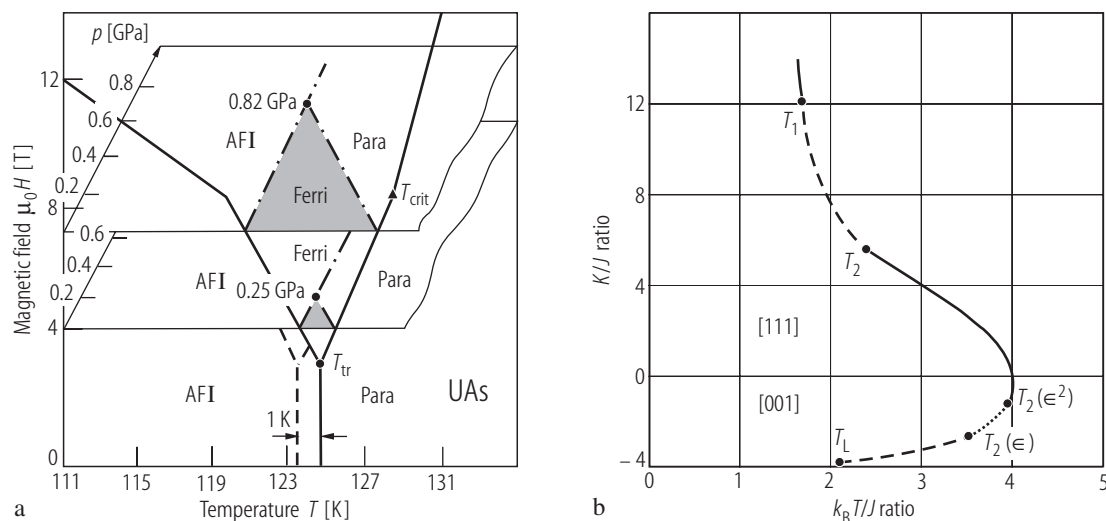


Fig. IV.37. UAs. (a) (T, H, p) MPD [85FT]. This diagram is a summary of the results on (T, H) -(Fig. IV.34) and (T, p) -(Fig. IV.35) magnetic phase diagrams. (b) The magnetic phase diagram with some correlations due to fluctuations (renormalization group approach) in the plane (K, T) , where K is the single-ion cubic anisotropy and T is the temperature [84S2]. UAs belongs to the systems which are described with $n \geq 2$ component Hamiltonian which exhibits the first-order phase transition even though the Landau theory predicts a continuous transition and the existing of a stable fixed point [77PM]. In the figure the solid lines and dashed (dotted) lines represent the second and the first-order phase

transitions, respectively, in ϵ -expansion to order $\epsilon(\epsilon^2)$ phase transition lines. The critical points T_1 and T_2 are independent of the ϵ -expansion. For details see the original paper. The T_L point ($K/J = -3.81$, $k_B T/J = 2.13$) is the intersection of the two transition lines mentioned above, the solid and dashed ones. The [111] and [001] directions designate the easy axes of given phases. The triple point T_{tr} ($T = 124.4$ K, $\mu_0 H = 3$ T) represents the coexistence of three phases :AFI, Ferri- and paramagnetic ones. Note that at T_{tr} the slopes dH/dT of the transition lines become different at 8 T.

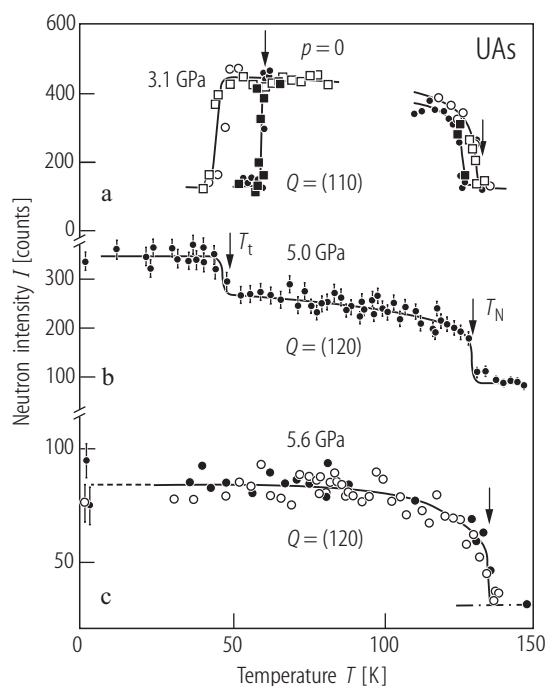


Fig. IV.38. UAs s.c. Neutron intensity, I , of the (110) or (120) peaks vs. temperature, T , measured for three different pressures, as indicated [95GMAL], [98BDGI]. ($T_N(p=0) = 127$ K). The upper frame gives the intensity of the magnetic reflection (110) (k_z -domain) under ambient pressure and 3.1 GPa, marked by closed and open symbols, respectively. Note an increase in T_N (by about 8 K) and decrease in the temperature T_t (by about 17 K), where T_t is the AF I \rightarrow AF IA first-order transition, under pressure. In the middle frame the data for 5 GPa show the transition at $T_t \approx 47$ K. The (120) magnetic reflection represents the k_y -domain. However, no step, except that at T_N , is observed at $p = 5.6$ GPa (lower frame).

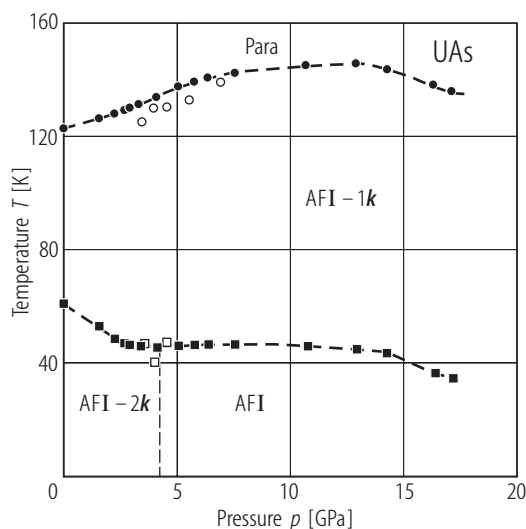


Fig. IV.39. UAs s.c. (T,p) magnetic phase diagram of UAs constructed on the basis of neutron diffraction (open symbols) and resistivity (closed symbols) measurements under pressure, respectively [98BDGI]. Note that T_N after initial linear increase with increasing pressure goes through a maximum at 14 GPa and then starts to decrease. There is given a speculation that the overall decrease in the conduction band susceptibility, χ_C , being enhanced for certain directions in k -space, is just responsible for the untypical change of the T_N vs. p dependence.

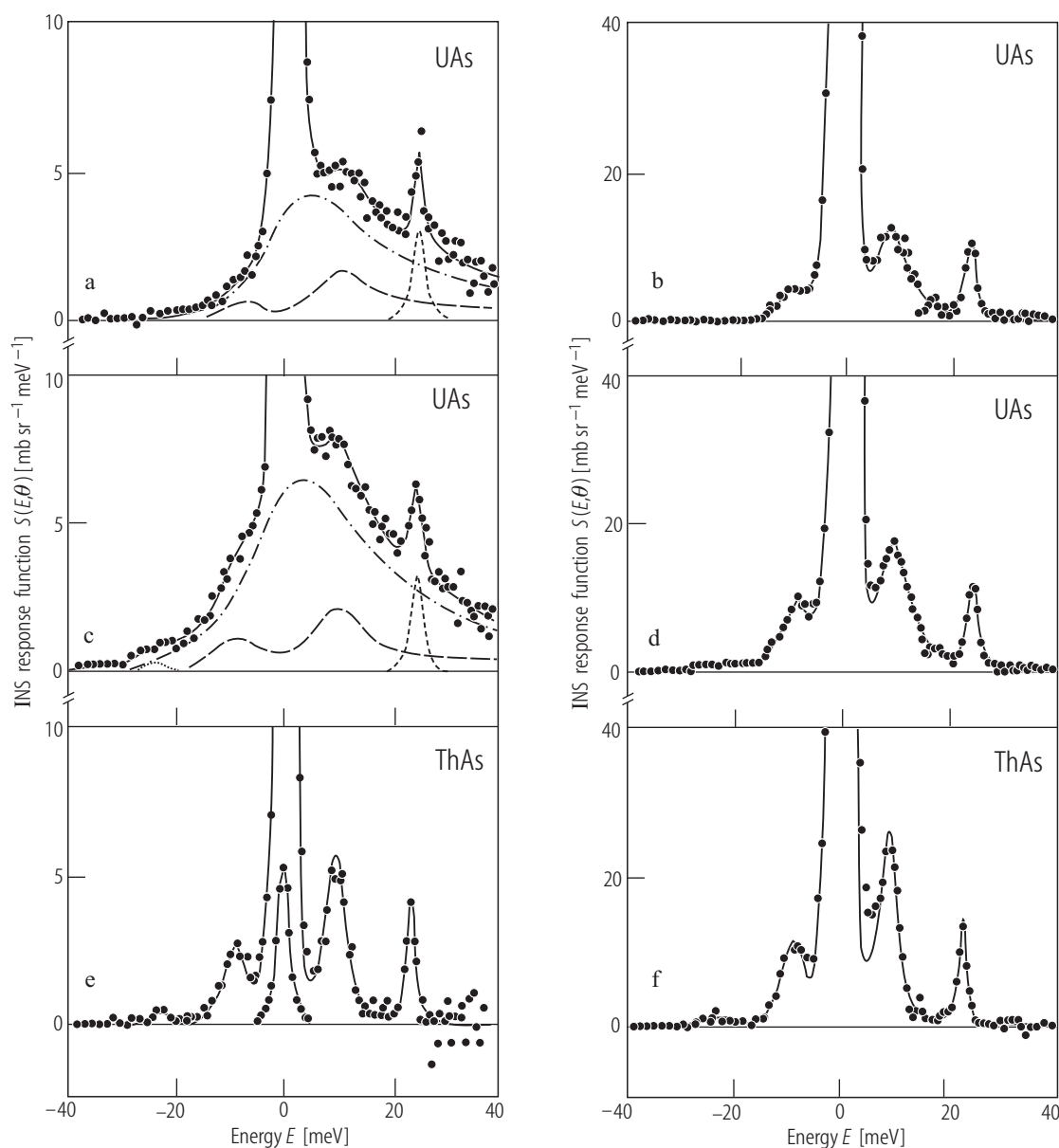


Fig. IV.40. UAs, (ThAs). The response spectroscopic function, $S(E, \theta)$, vs. neutron scattering energy, E , for constant angle θ (a) and (b) UAs, $T = 80$ K; (c) and (d) UAs, $T = 150$ K; (e) and (f) ThAs, $T = 150$ K [82LLMM]. Plots on the right ($Q = 9.2 \text{ \AA}^{-1}$) are acoustic and optic phonons while plots on the left ($Q = 0.9 \text{ \AA}^{-1}$) are magnetic scattering and phonons for UAs and phonons for ThAs. Solid curves are fits to the data. In the case of UAs the neutron data are deconvoluted into phonon (dashed curve) and magnetic (chain curve) contributions. Energies and HWHM of Lorentzians applied to fit phonons are in the Table:

Compound	Acoustic phonons		Optical phonons	
	E [meV]	$1/2\Gamma$ [meV]	E [meV]	$1/2\Gamma$ [meV]
UAs	9(1)	2.8(5)	24.1(5)	0.8(2)
UAs s.c.*	8...10		24.4	
ThAs	9(1)	1.3(2)	23.3(5)	0.4(1)

*) [80SLV].

No sharp excitations or crystal-field levels are observed below 30 meV. The lack of the latter is in contrast to the results of [77FMV]. Instead, a broad quasi-elastic contribution as a function of temperature is shown in figure c) spectrum taken in the paramagnetic state.

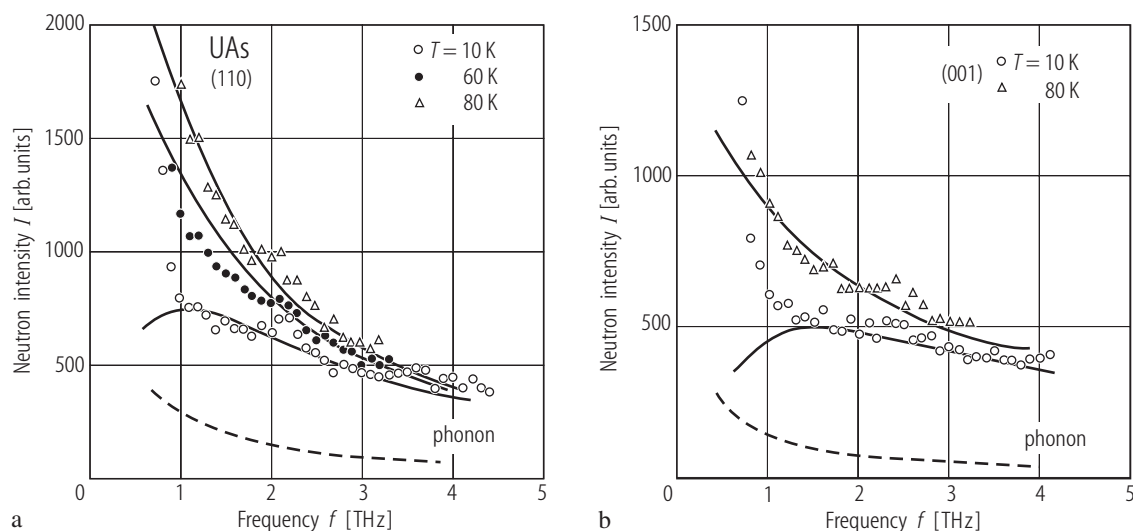


Fig. IV.41. UAs s.c. (a) Inelastic neutron scans for $Q = (110)$ measured at three different temperatures (indicated) compared to the phonon contribution at 80 K [81L]. (b) The same for $Q = (001)$ but measured at two different temperatures as indicated [81L]. For both figures the solid curves represent the variation in scattering expected if the

overall scale factors $\chi(110) = 700$ and Lorentzian energy distribution $\Gamma(110) = 1.1$ THz (figure (a)) and correspondingly $\chi(001) = 400$ and $\Gamma = 1.6$ THz (figure (b)). No collective excitations are indicated in the ordered state. There is also a considerable increase in the scattering with increasing temperature. See also [80SLV].

For Fig. IV.42 see next page

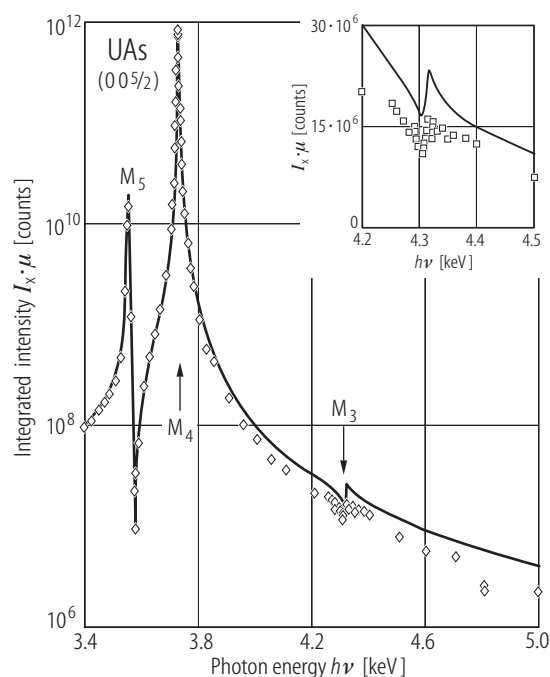


Fig. IV.43. UAs s.c. RXMS: The intensity times the absorption coefficient, $I_x \cdot \mu$ of the (0,0,5/2) satellite as a function of photon energy $h\nu$ from 3.4 up to 5 keV (open diamonds) through the M_5 (3.552 keV), M_4 (3.728 keV) and M_3 (4.303 keV) absorption edges [90MVII]. The solid line is a fit to the coherent sum of three quantum-mechanical dipole oscillators. For the theoretical considerations see the original work. The inset shows an expanded view of the M_3 edge. See also [98M].

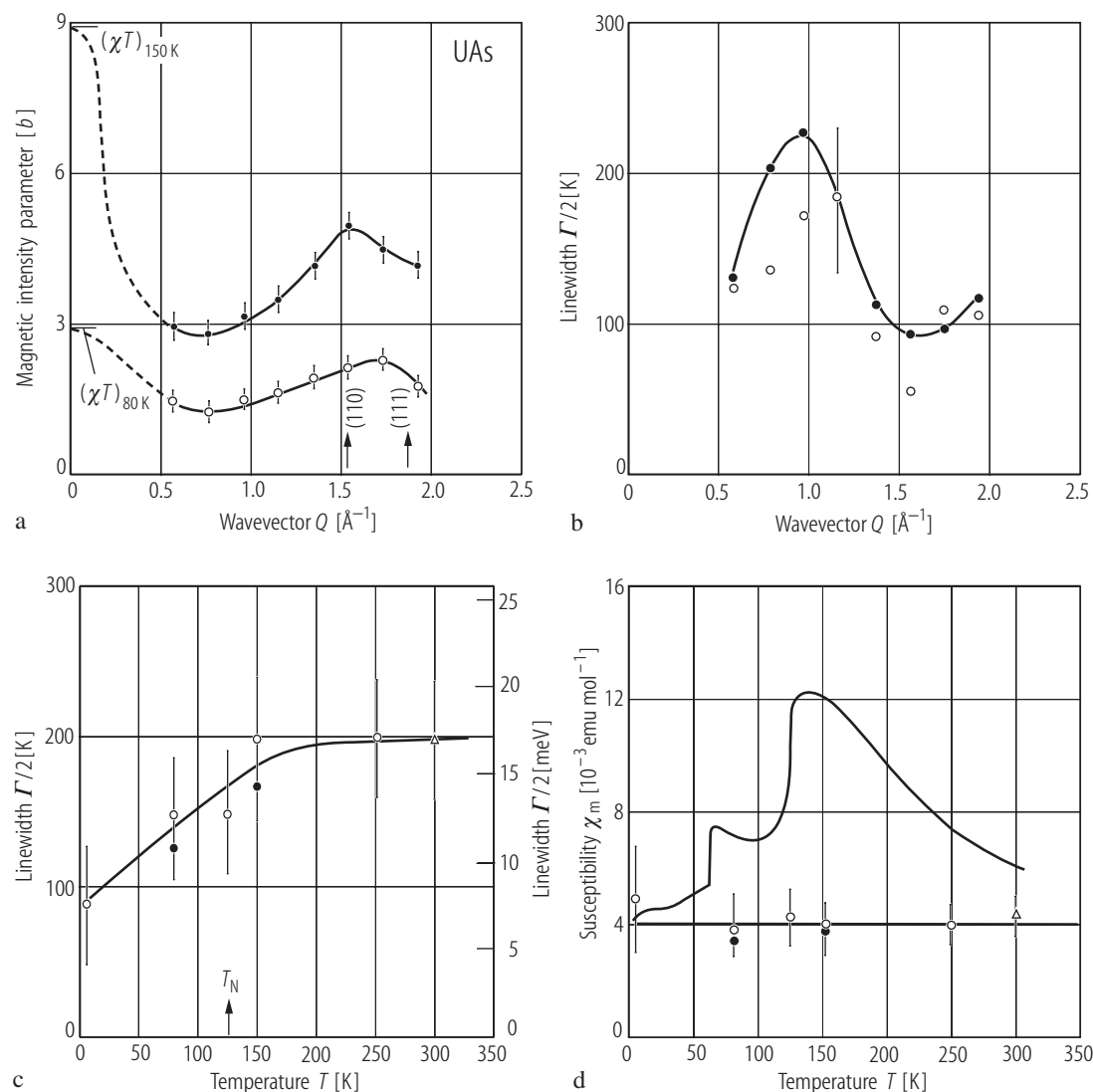


Fig. IV.42. UA5. **(a)** Intensity parameter being related to the product of the static susceptibility $\chi(Q)$ and the temperature, T , and **(b)** the HWHM linewidth ($\Gamma/2$) of magnetic scattering as a function of scattering vector Q [82LLMM]. The data are for two temperatures 80 K (open circles) and 150 K (closed circles). The solid curves are a guide to the eye, while the dashed curves connect the neutron scattering results with the $Q = 0$ bulk susceptibility taken from [74TL]. Note a clear trend of the intensity at both temperatures, i.e. in the ordered and paramagnetic state to increase with going from the zone center to the zone boundary. The maximum near the (110) zone boundary is caused by the antiferromagnetic correlations (see also [80SLV]). **(c)** Average HWHM of magnetic inelastic scattering, $\Gamma/2$, vs. temperature, T , [82LLMM]. The values are obtained by

fitting the data with a Lorentzian centered at $\hbar\omega = 0$ for $0.6 \leq Q \leq 0.8 \text{ \AA}^{-1}$ using different samples of UA5 and spectrometers which is marked by the different symbols. The solid curve is a guide to the eye. The result obtained can be only explained by taking into account some aspects of intermediate valence behaviour of uranium in describing its ground-state wave functions. **(d)** Static molar magnetic susceptibility, χ_m , (taken from [74TL]) vs. temperature, T , (solid line) compared to the values determined from the integrated (over energy) neutron intensity of magnetic scattering at the scattering vector $Q = 0.7 \text{ \AA}^{-1}$ (symbols). Note that at this point $\chi(Q)$ is essentially constant against temperature in contrast to the bulk susceptibility. This discrepancy is probably a consequence of ferromagnetic correlations [82LLMM].

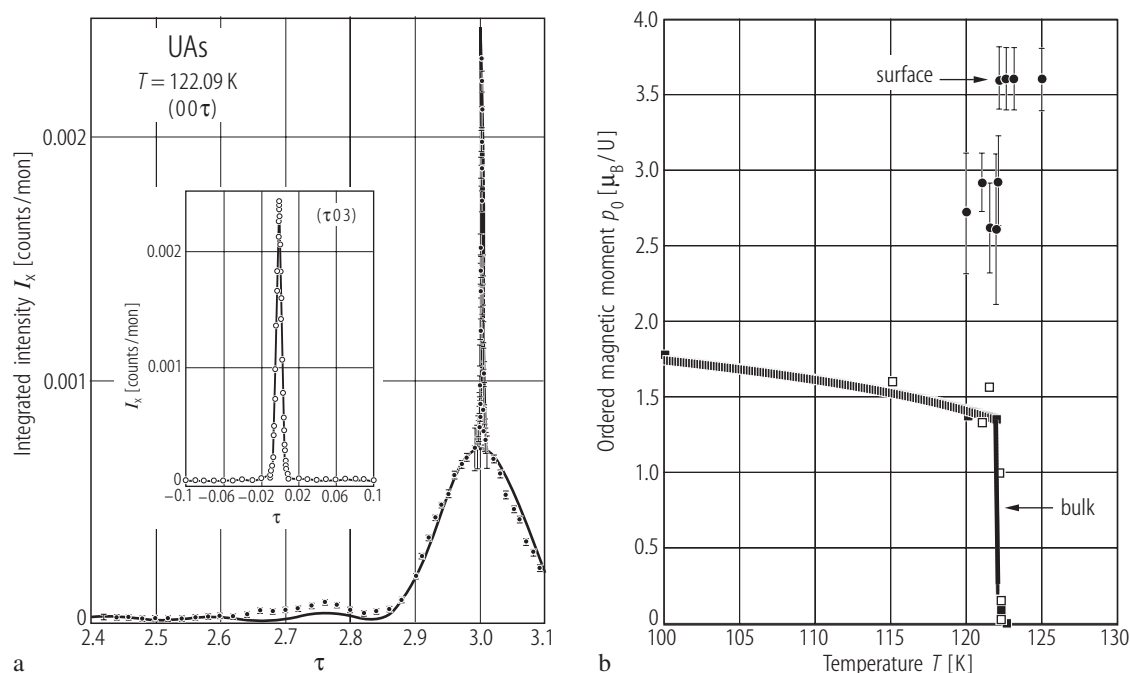


Fig. IV.44. UAs s.c. RXMS: M_4 absorption edge (examination of the first-order AF phase transition at T_N). **(a)** The integrated intensity of X-ray scattering, I_x , measured perpendicular and parallel to the surface vs. reciprocal vector along the $(0,0,\tau)$ (figure) and along $(\tau,0,3)$ (inset) directions [95BSVD]. The extremely narrow and very broad components of the response correspond to the onset of bulk

antiferromagnetism and the surface one, respectively. The solid line is the result of a model calculation which takes into account 11 surface- and approximately 600-bulk magnetic layers. **(b)** Surface and bulk ordered magnetic moment per U atom, p_0 , vs. temperature, T , close to T_N [95BSVD]. The heavy line is a result of a Landau free energy model for the first-order transition.

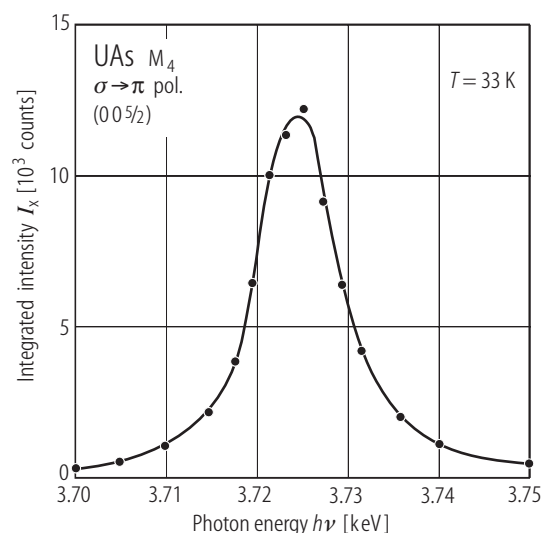


Fig. IV.45. UAs s.c. RXMS: Total resonance integrated intensity, I_x , vs. photon energy $h\nu$. The σ to π polarization of the $(0,0,5/2)$ magnetic peak through the M_4 absorption edge of uranium [89IMPI]. A resonant enhancement is of a factor of $8 \cdot 10^6$. The magnitude and polarization of the data are in qualitative agreement with the theory of [88HTBG].

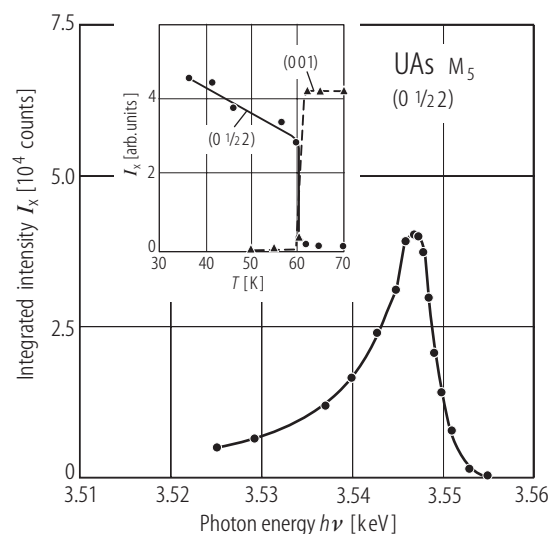


Fig. IV.46. UAs s.c. RXMS: Total integrated resonance intensity, I_x , vs. photon energy $h\nu$ of incident X-rays at the M_5 absorption edge of uranium taken at the temperature of the magnetic phase transition $T_i \approx 60$ K. The lower value of T_i arises from the given experimental condition [89IMPI]. In the inset, the transition from type-I to type-IA structure is illustrated by the vanishing of the intensity of the $(0, 1/2, 2)$ magnetic peak when going from low to high temperatures. The magnetic scattering intensity is only $\sim 0.01\%$ of the intensity at the $(0, 0, 2)$ charge peak, which gives 10^5 times larger intensity than the expected non-resonant magnetic scattering intensity (FWHM = 10 eV). This arises from strong electric multiple transitions between atomic core states (3p, 3d) and the exchange split Fermi-edge states (6d, 5f) (see [88HTBG]). The asymmetry of the M_5 line arises from interference with the low energy tail of the M_4 resonance.

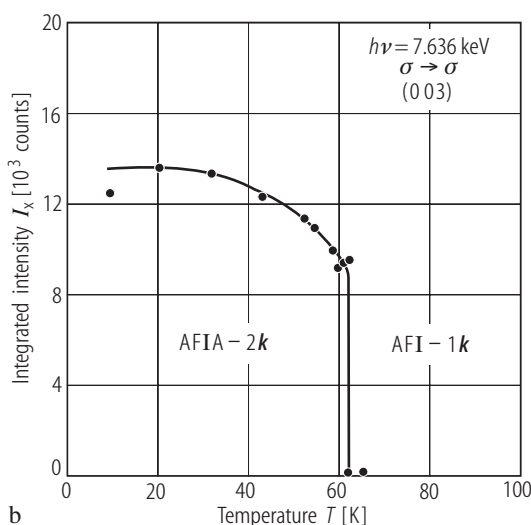
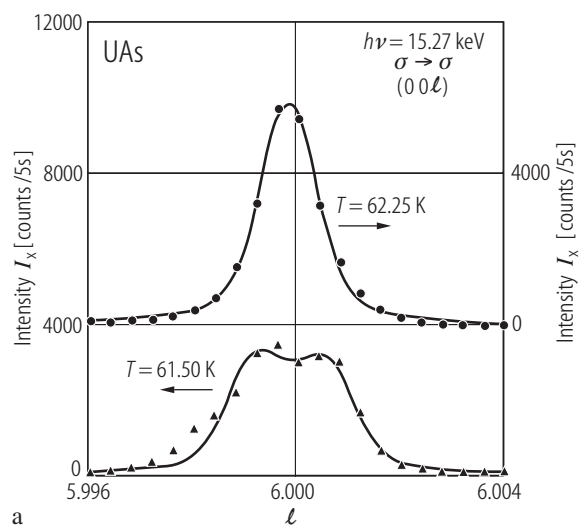


Fig. IV.47. UAs s.c. RXMS: **(a)** Radial X-ray scans through the (006) peak, corresponding to the (003) peak if synchrotron radiation is $\lambda/2$ at temperatures slightly above (upper panel) and below (lower panel) T_N [90MVII]. Note a splitting of the (006) reflection occurring at $T < T_N$. The data can be fit to two overlapping reflections with the same width but at positions that differ by $\delta c^* = 0.0015c^*$. The c/a

ratio in the tetragonal phase is greater than one. **(b)** A nonallowed Bragg peak intensity, I_x , of $(003)^{\sigma-\sigma}$ vs. temperature, T , attributed to a charge modulation at 2τ , where τ is the wave vector of the magnetic modulation, observed in the stability region of the type-IA-double k structure, i.e. below 61.5 K [90MVII].

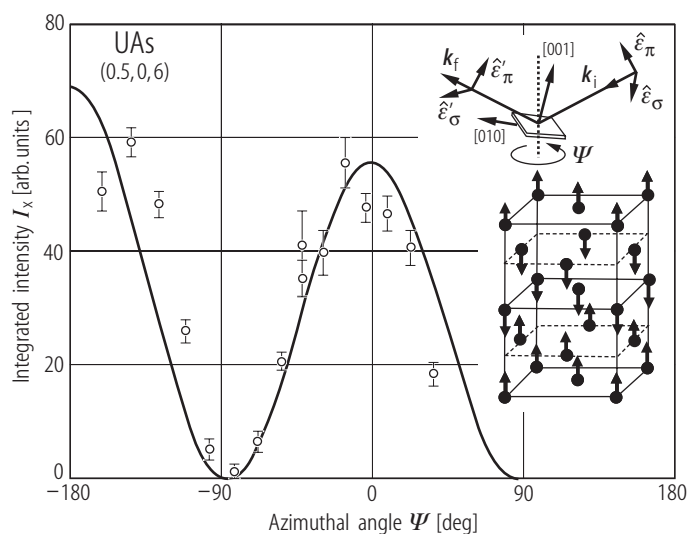
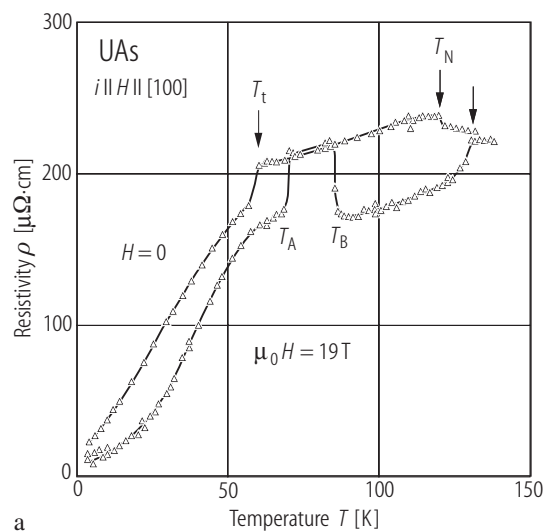


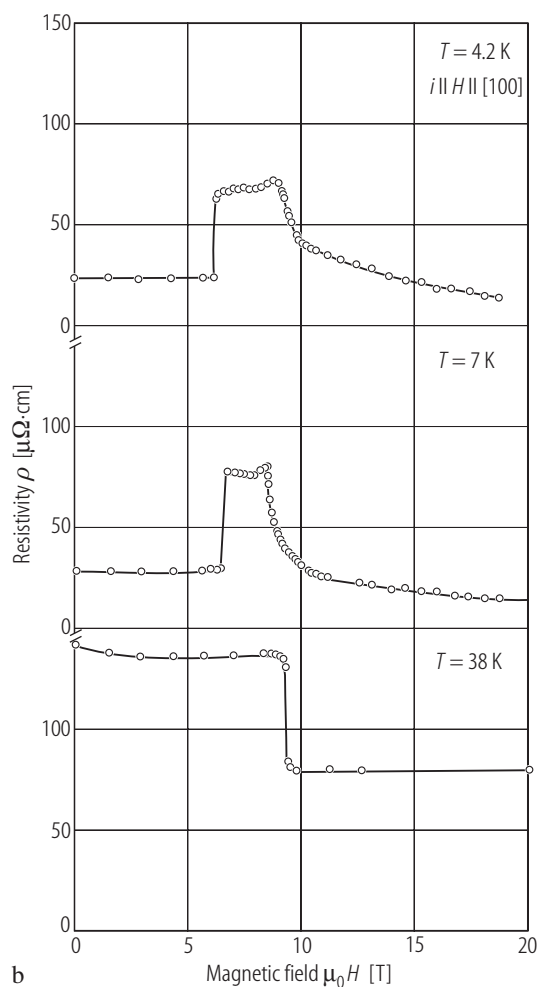
Fig. IV.48. UAs s.c. RXMS: Measurements at the As K edge. Integrated intensity, I_x , in the $\sigma \rightarrow \pi$ channel of the $(1/2, 0, 6)$ reflection at 20 K as a function of the azimuthal angle, ψ , around the normal to the $[001]$ direction (see the upper inset) [01MSBP]. The azimuthal angles $\psi = 0$ and 180° correspond to the $[100]$ axis, lying in the scattering plane. Close to the As K-edge energy intensities abnormally increase up to $8 \cdot 10^4$ counts/s in full polarization mode. The observed scattering angle dependences of the Bragg intensities are consistent with the proposed E1 dipole symmetry (solid line) from 1s to 4p states of the scattering potential (see the original paper). The lower inset shows the AF IA-type-1 k magnetic structure.

For Fig. 49 see next page



a

Fig. IV.50. UAs s.c. (a) Electrical resistivity, ρ , vs. temperature, T , measured at $\mu_0 H = 0$ and 19 T with the electrical current flowing parallel to the $[100]$ direction [87TFSV]. T_A and T_B are transition temperatures (compare with MPD in Fig. IV.31). Although the shape of the resistivity curves is the same as in previous works [74TK] or [84SFV], the resistivity changes at the transition temperatures have an opposite sign, due to the large sensitivity into internal stresses in different samples. (b) Electrical resistivity, ρ , vs. applied magnetic fields up to 10 T measured at three different temperatures: 4.2, 7 and 38 K within the temperature range, where the AF IA-2 k magnetic structure is stable [87TFSV]. Note, that no domain wall motion occurs up to the highest field of stability of the AF IA-2 k phase, i.e. ~ 9 T at $T = 38$ K. As is the case of UP (Fig. III.38a), an abrupt decrease of ρ takes place at the Ferri-AF IA-2 k transition (see MPD of UAs in Fig. IV.31).



b

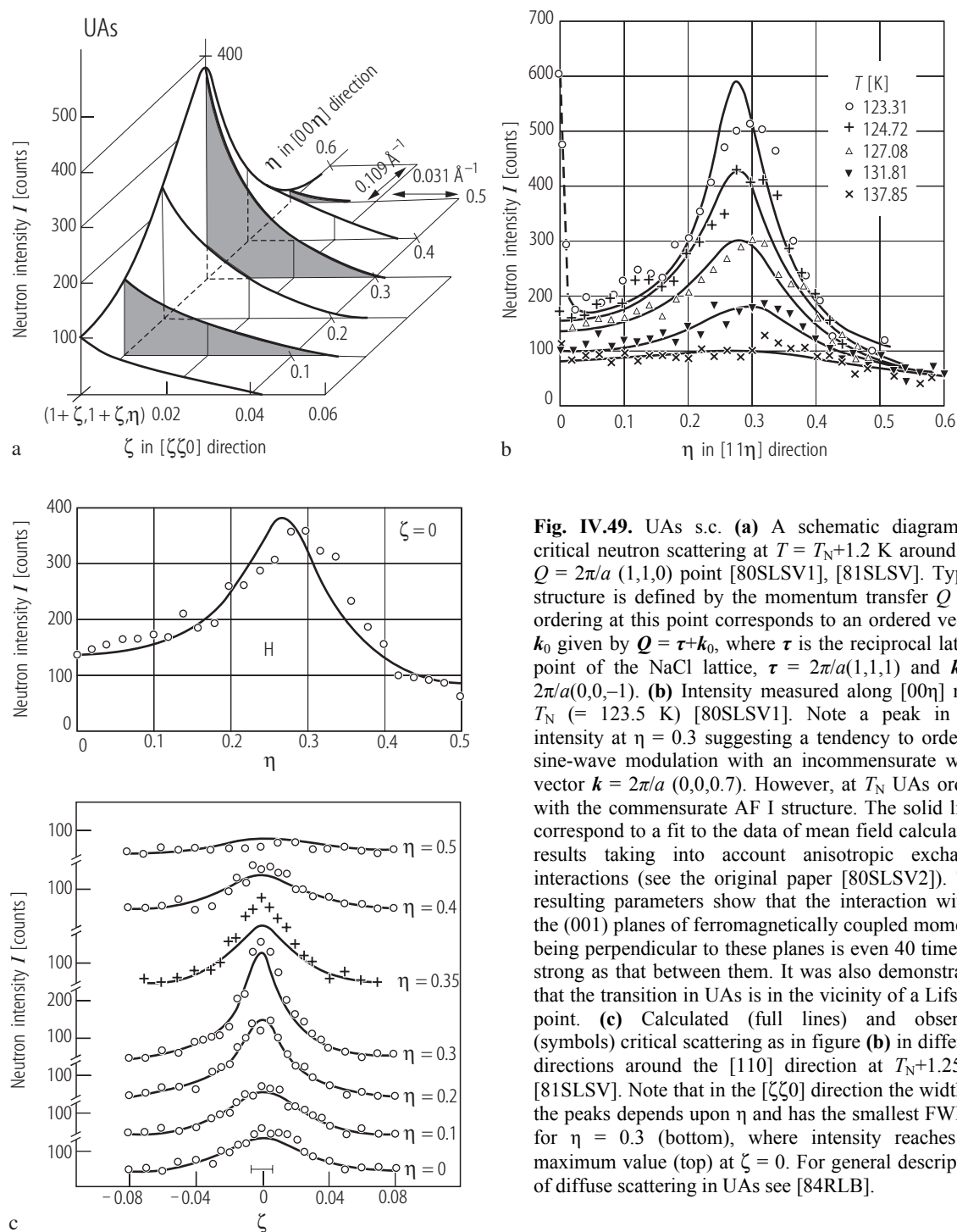


Fig. IV.49. UAs s.c. **(a)** A schematic diagram of critical neutron scattering at $T = T_N + 1.2$ K around the $Q = 2\pi/a(1,1,0)$ point [80SLSV1], [81SLSV]. Type I structure is defined by the momentum transfer Q and ordering at this point corresponds to an ordered vector k_0 given by $Q = \tau + k_0$, where τ is the reciprocal lattice point of the NaCl lattice, $\tau = 2\pi/a(1,1,1)$ and $k_0 = 2\pi/a(0,0,-1)$. **(b)** Intensity measured along $[00\eta]$ near T_N ($= 123.5$ K) [80SLSV1]. Note a peak in the intensity at $\eta = 0.3$ suggesting a tendency to order in sine-wave modulation with an incommensurate wave vector $k = 2\pi/a(0,0,0.7)$. However, at T_N UAs orders with the commensurate AF I structure. The solid lines correspond to a fit to the data of mean field calculation results taking into account anisotropic exchange interactions (see the original paper [80SLSV2]). The resulting parameters show that the interaction within the (001) planes of ferromagnetically coupled moments being perpendicular to these planes is even 40 times as strong as that between them. It was also demonstrated that the transition in UAs is in the vicinity of a Lifshitz point. **(c)** Calculated (full lines) and observed (symbols) critical scattering as in figure (b) in different directions around the $[110]$ direction at $T_N + 1.25$ K [81SLSV]. Note that in the $[\zeta\zeta 0]$ direction the width of the peaks depends upon η and has the smallest FWHM for $\eta = 0.3$ (bottom), where intensity reaches its maximum value (top) at $\zeta = 0$. For general description of diffuse scattering in UAs see [84RLB].

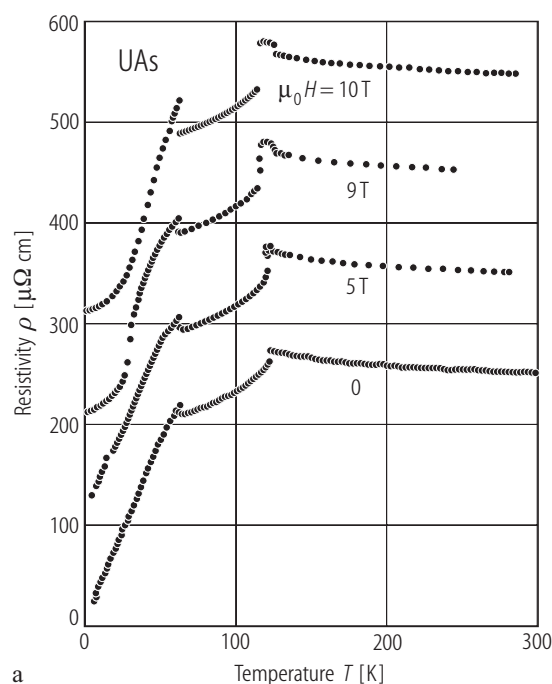
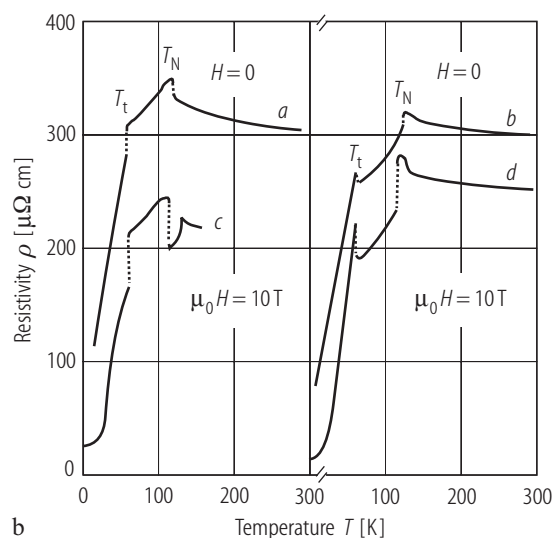


Fig. IV.51. UAs s.c. **(a)** Electrical resistivity, ρ , vs. temperature, T , in magnetic fields up to 10 T applied along the [001] direction [84SFV]. For clarity, the curves are shifted by 100 $\mu\Omega\text{cm}$. $T_N = 123(1)$ K, $T_t = 64(1)$ K at $H = 0$. Note that below 50 K the resistivity varies linearly with temperature and remains unchanged upon application of fields up to 5 T. At higher fields, at about 10 T there is a transition from AF IA- $2k$ to Ferri- $2k$, which manifests itself in a larger peak at the transition and deviation from the straight line behaviour below this transition. Above this temperature it goes through two maxima at T_t and T_N which can be explained by taking into account the formation of a new Brillouin-zone due to the different periodicity of the magnetic structure in respect to the crystallographic unit



cell. The overall shape of $\rho(T)$ is reminiscent to that presented at the first such a study on an arc-melted sample in [74TK]. **(b)** The ρ vs. T plots in zero field measured by: (curve a) [87BBTT] (left hand panel) and (curve b) [84SFV] (right hand panel) compared to such plots taken at 10 T by (curve c) [87TFSV] with $i \parallel H$ and (curve d) [84SFV] with $i \perp H$. For clarity the curves a and b have been shifted by 50 $\mu\Omega\text{cm}$ [87BBTT]. Note quite different behaviour of the temperature variation at the transition points T_t and T_N . These results indicate that the electrical resistivity is very sensitive to uniaxial stress and is just attributed to the magnetic domain rearrangement under stress.

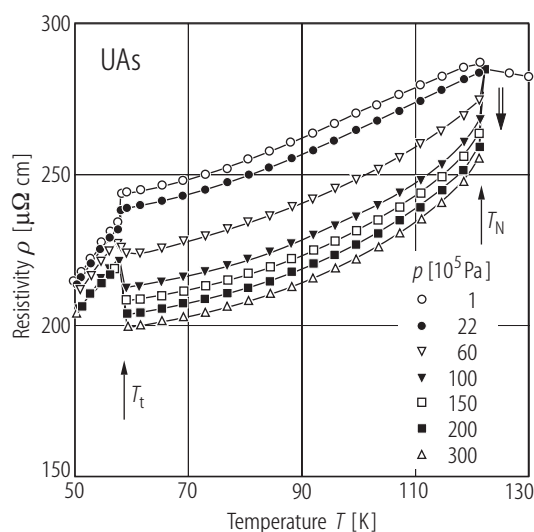


Fig. IV.52. UAs s.c. Electrical resistivity, ρ , vs. temperature, T , in the range 50...130 K for different applied stress parallel to the electric current along the [001] axis [90BBTN], [93FG]. The phase occurring below T_t is antiferromagnetic, double- k type IA, while that between T_t and T_N is antiferromagnetic, single- k type I. Note the decrease of ρ under applied stress at T_N (double arrow), while for the same type of magnetic structure in UP, its value increases (see Fig. III.40). Stress effects measured with stress applied parallel to the [001] axis and perpendicular to the electric current are small in comparison to those shown in the figure.

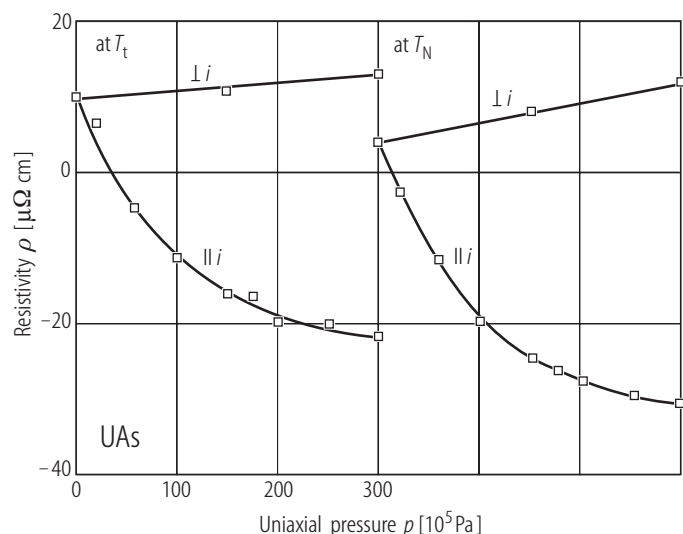


Fig. IV.53. UAs s.c. Electrical resistivity, ρ , measured at the transition temperatures T_t and T_N under stresses applied parallel or perpendicular to the electric current direction [87BBTT]. Note that the effects are opposite in sign and much larger under parallel stress what makes ρ in the ordered phases of UAs very sensitive to an uniaxial stress, especially applied parallel to the electric current. These effects are attributed to the magnetic domain rearrangement under stress.

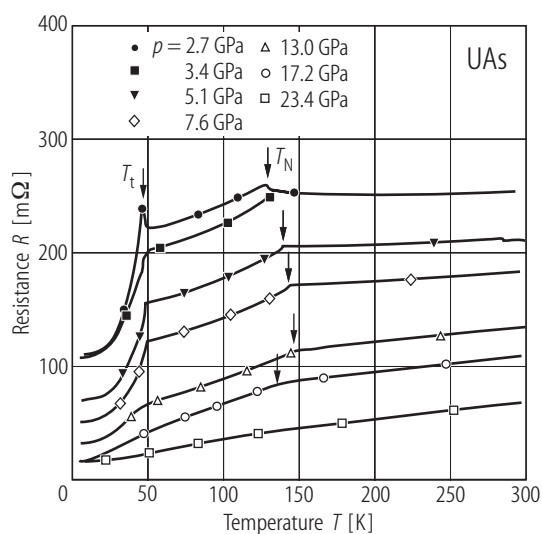


Fig. IV.54. UAs s.c. Electrical resistance, R , vs. temperature, T , measured at various pressures, p , from 2.7 to 23.4 GPa [98BDGI]. Note that the transition AF I \rightarrow AF IA is not seen at pressures above 5.0 GPa, as it was observed in neutron diffraction experiment under 5.6 GPa pressure [95GMAL] (see Fig. IV.38).

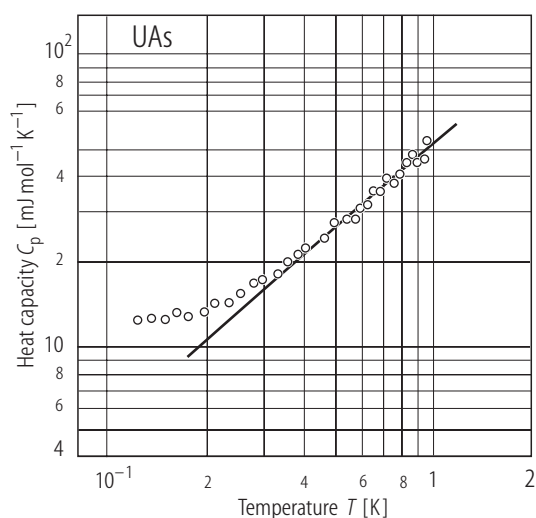


Fig. IV.55. UAs s.c. A log-log plot of heat capacity C_p vs. temperature, T , below 1 K [85ROV2]. The solid line reflects the experimental data taken above 1.5 K and fitted to the equation: $C_p = C_{el} + C_L = \gamma(0)T + \beta T^3$, $\gamma(0) = 53.20(15) \text{ mJ/mol K}^2$, $\Theta_D = 221(2) \text{ K}$. The same $\gamma(0)$ -value was reported in [80BTLM]. For $C_N(T)$ see Fig. R.40a.

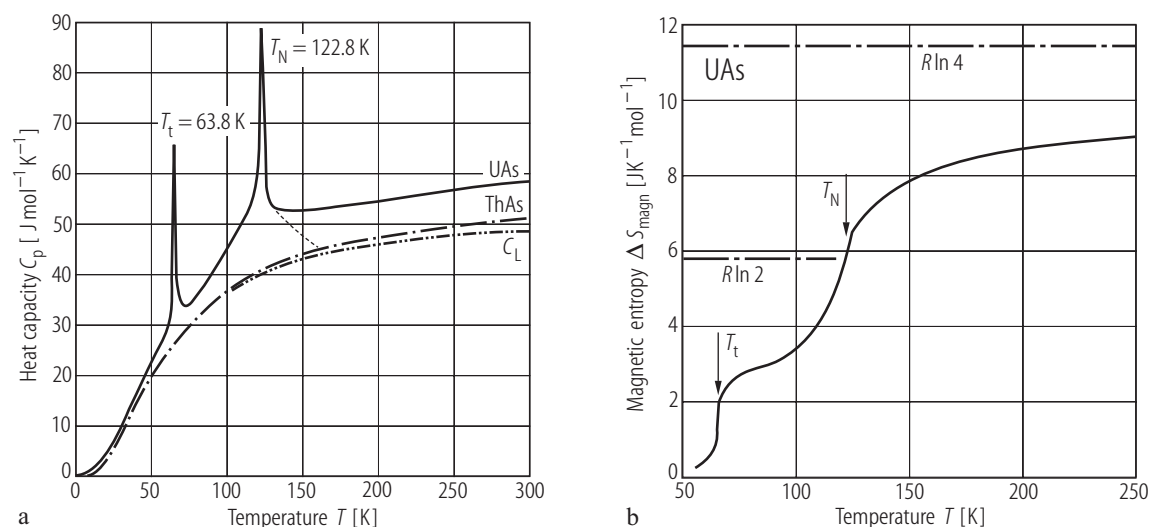


Fig. IV.56. UAs, (ThAs). **(a)** Heat capacity C_p vs. temperature, T , measured for UAs and its nonmagnetic counterpart ThAs [80BTLM]. The double-dot dashed lines C_L represents the estimated lattice heat capacity of UAs. Note two sharp anomalies associated with the magnetic transitions at T_t ($= 63.8$ K) and T_N ($= 122.8$ K). **(b)** Total magnetic entropy, ΔS_{magn} , vs. temperature, T , [80BTLM].

Taking into account the U^{3+} ion ($5f^3$) with main ground term component $^4I_{9/2}$, one gets its splitting in the octahedral crystal field to one doublet Γ_6 and two quadruplets Γ_8 . The ΔS_{magn} value at T_N supports rather a doublet as a ground state, which is not consistent with other predictions of quadruplet as a ground state. At higher temperature of 250 K ΔS_{magn} is only $0.8 R \ln 4$.

For Fig. IV.57 see next page

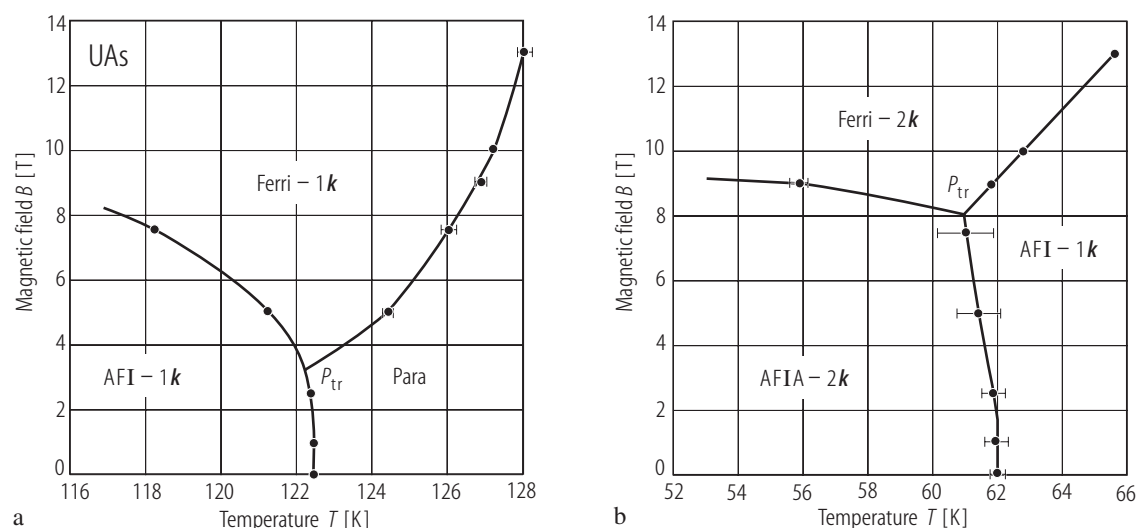


Fig. IV.58. UAs s.c. (B , T) MPD: The hysteresis effect of the transitions measured around **(a)** T_N and **(b)** T_t by heat capacity C_B measured in a magnetic field [03PJBS]. The bars indicate the difference in the transition temperature detected upon cooling and heating. The solid lines connect the averaged values of the transition temperatures.

The triple point P_{tr} for AF I-1k/ Ferri-2k/ AF IA-2k phases is located at $T_{tr} = 61.5$ K and $B_{tr} = 8.54$ T, while that for Para/ Ferri-1k/ AF I-1k at $T_{tr} = 122.4$ K and $B_{tr} = 3.1$ T. Note that measurable hysteresis is found only for the Para/ Ferri-1k **(a)**, AF I-1k/ AF IA-2k and AF IA-2k/ Ferri-2k **(b)** phase transition lines.

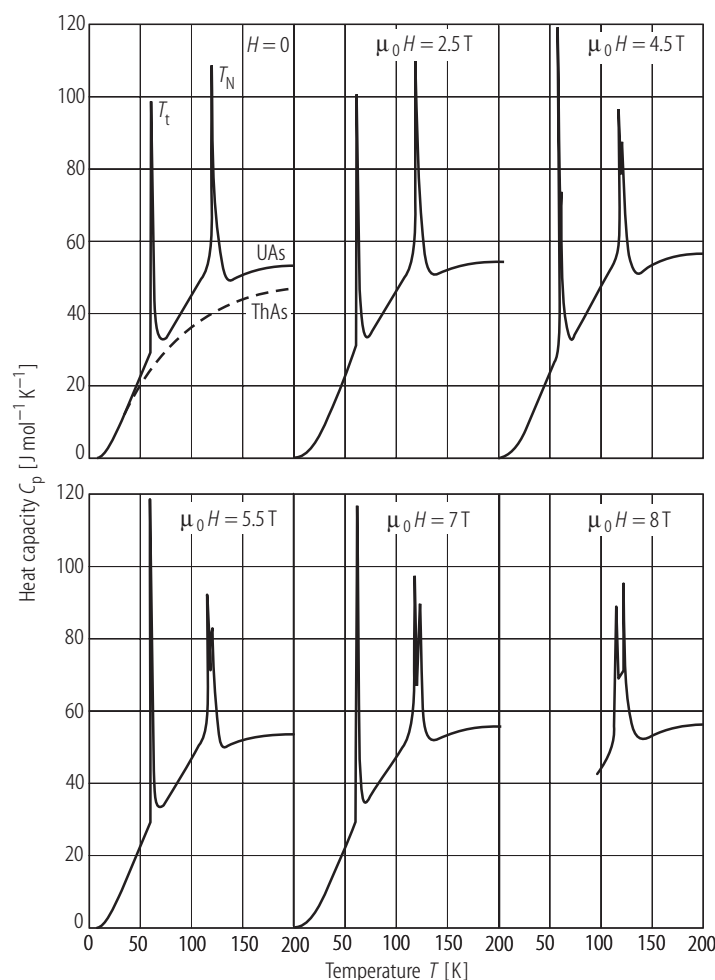


Fig. IV.57. UAs s.c. Heat capacity, C_p , vs. temperature, T , measured in various magnetic fields applied along the [100] axis (indicated) [80RBBT]. The dashed line is the thermal variation of C_p for ThAs taken from [80BTLM]. Note that the peak observed at T_N ($H = 0$) is divided into two peaks in higher magnetic fields and its temperature splitting increases with the field as the magnetization does. The magnetic entropy jump, $\Delta S_{\text{magn}}/R$, ($= 0.53$) at T_N is almost the same as that deduced from the Clapeyron relation ($\Delta S_{\text{magn}}/R = 0.58$) using magnetization data.

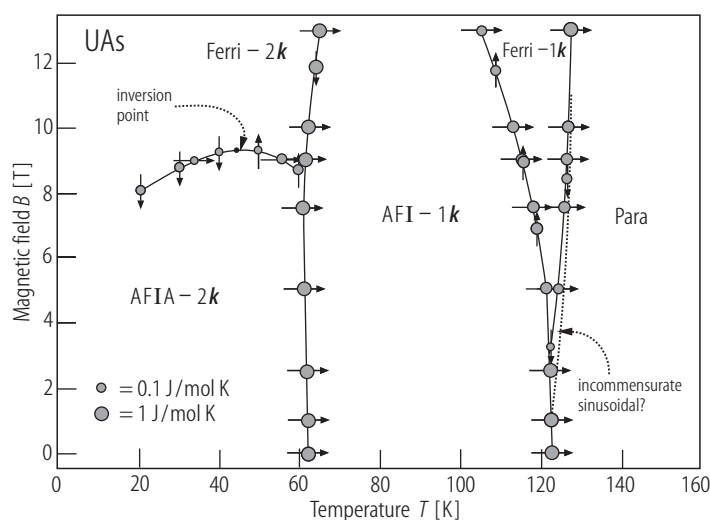


Fig. IV.59. UAs s.c. (B, T) magnetic phase diagram based on the specific heat (C_B) and isothermal magnetocaloric measurements, (M_T), presented in Figs. IV.60...63 [03PJBS]. The arrows indicate the direction of the entropy increase (horizontal arrows – based on C_B , vertical ones on M_T), while the size of each circle is proportional to the logarithm of the entropy jump at a given point. The dotted line denotes a second order transition into the hypothetical incommensurate - sinusoidally modulated phase detected only in magnetocaloric experiment. One sees the inversion point for the AF IA- $2k$ / Ferri- $2k$ transition at 46 K and $B = 9.30 \text{ T}$. Since the magnetization jumps remain almost unchanged at the transition AF IA- $2k$ / Ferri- $2k$ phase line (see [79BVB]), hence one can regard the transition at the inversion point as a first-order phase transition with zero latent heat. Compare this MPD with that presented in Fig. IV.31, determined by magnetic and neutron diffraction studies.

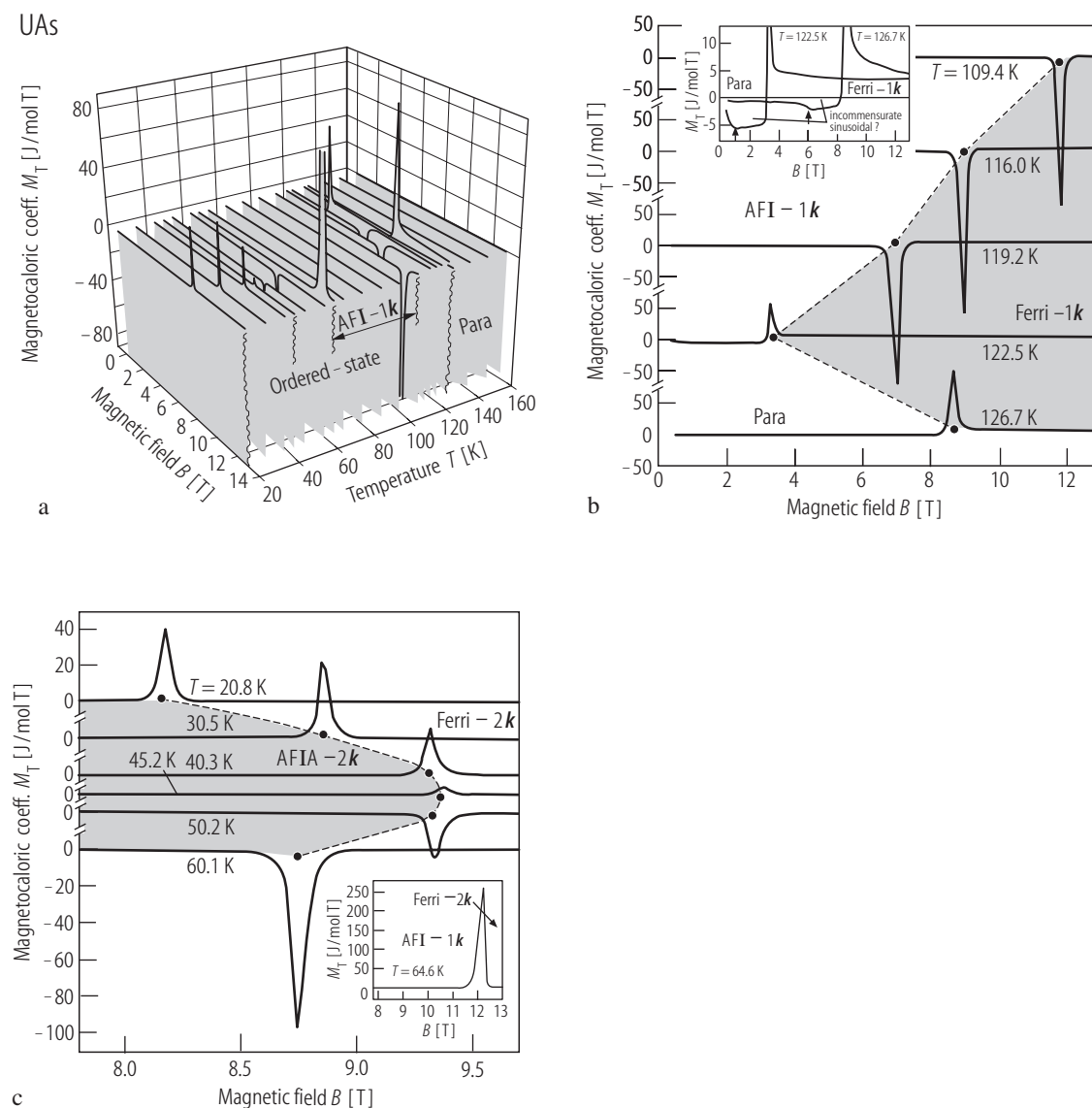


Fig. IV.60. UAs s.c. **(a)** The isothermal magnetocaloric coefficient, M_T , measured at various temperatures, T , and upon increasing magnetic fields up to 13 T [03PJBS]. Just above the Para/ ordered state transition $M_T = -0.6$ J/mol T at $B = 0$ and $M_T = -0.9$ J/mol T at $B = 13$ T. Note that both positive and negative peaks are observed, corresponding to negative or positive entropy jumps ΔS upon increasing magnetic field, respectively. Note also that in the range of the AF I-1k phase M_T was not detected. The sign of ΔS agrees with the Clausius-Clapeyron law (see Fig. IV.59). **(b)** A magnification of the field region, where M_T changes in the vicinity of the transition from the AF I-1k, or the paramagnetic phase to the Ferri-1k phase [03PJBS]. According to the predictions, M_T for the Para/ Ferri-1k

phase is positive. The inset shows M_T at two temperatures (indicated) in the case of the formation of an incommensurate, sinusoidally modulated phase just about 2 T below the Para/ Ferri-1k phase transition (arrows) being of a second-order transition. However the transition from the incommensurate to commensurate phase, or AF I \rightarrow AF IA is of first order due to the closeness to the Lifshitz instability. **(c)** A magnification of the region where the inversion at 46.0 K and $B = 9.3$ T on the AF IA-2k/ Ferri-2k phase transition line takes place. The inset shows a $M_T(B)$ curve at the AF I-1k/ Ferri-2k transition, where a large negative jump of the entropy is observed (recall opposite change of M_T with respect to ΔS) [03PJBS].

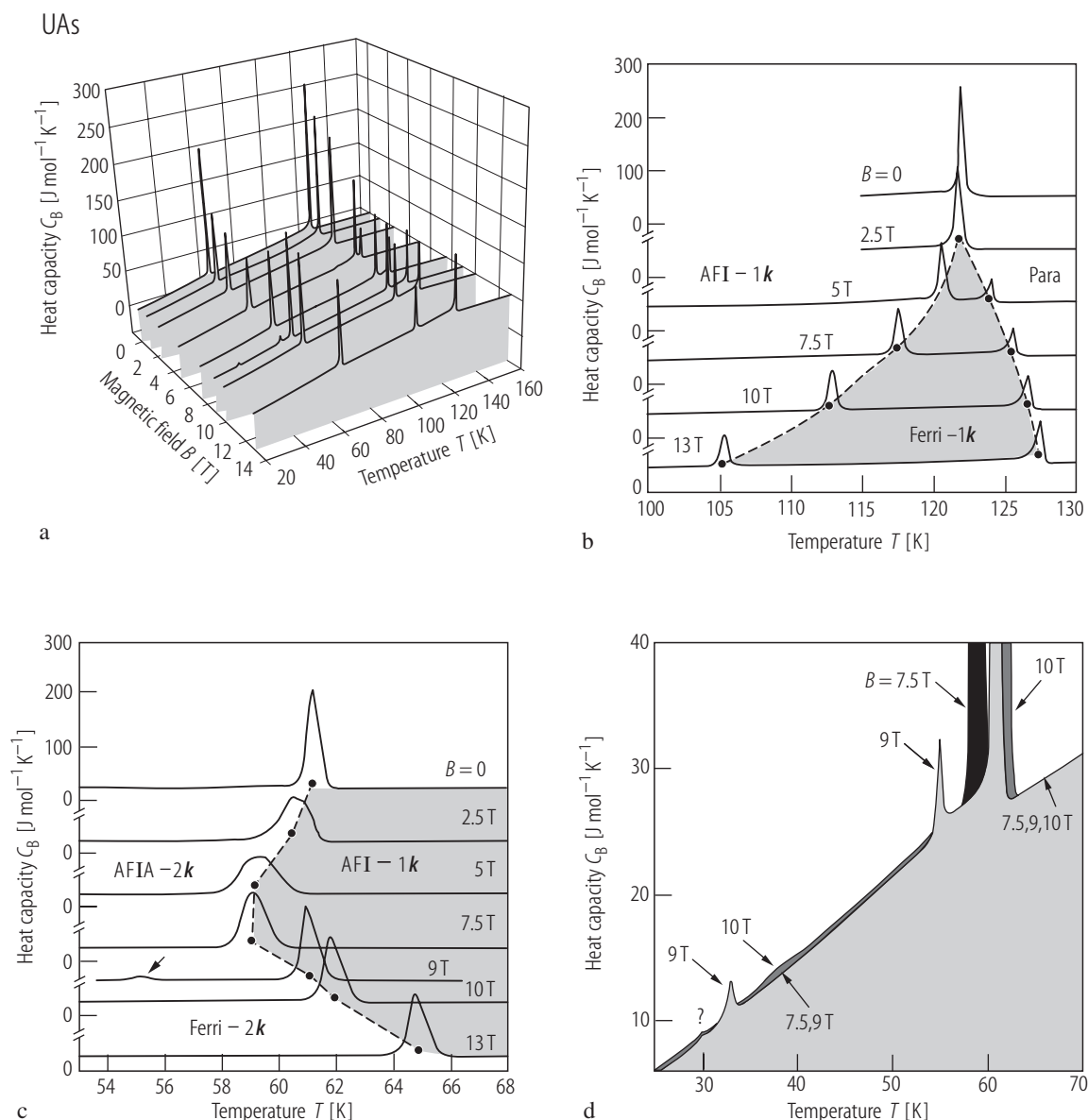


Fig. IV.61. UAs s.c. **(a)** Heat capacity, C_B , taken for various values of magnetic field, B , up to 13 T, (oriented $B \parallel a$) and temperatures $T = 20 \dots 160$ K in runs upon cooling [03PJBS]. Note a number of first-order transitions but especially for the curve for $B = 9$ T for which as many as five transitions were detected. **(b)** A magnification of the high-temperature region where a single peak of the Para/ AF I-1k transition above 3.1 T splits into two, attributed with the Para/ Ferri-1k and Ferri-1k/ AF I-1k transitions. No precursor effect is observed [03PJBS]. **(c)** A magnification of the low-temperature region, where the AF I-1k/ AF IA-2k reordering transition takes place [03PJBS]. As seen, this

transition first moves to lower temperatures with increasing magnetic field and with accompanying increase of the transition width. However above $B > 9.3$ T, the tendency is opposite, and finally the transition temperature exceeds that found for zero field. **(d)** Heat capacity, C_B , vs. temperature, T , measured upon cooling in the low-temperature region in applied magnetic fields $B = 7.5, 9$ and 10 T [03PJBS]. Note at 9 T three transitions at 1) 33, 2) 55 and 3) 60 K, corresponding to the Ferri-2k/ AF IA-2k/ AF I-1k magnetic structure transformations, respectively. The small feature at 30 K is unknown ($\text{UO}_2?$).

UAs

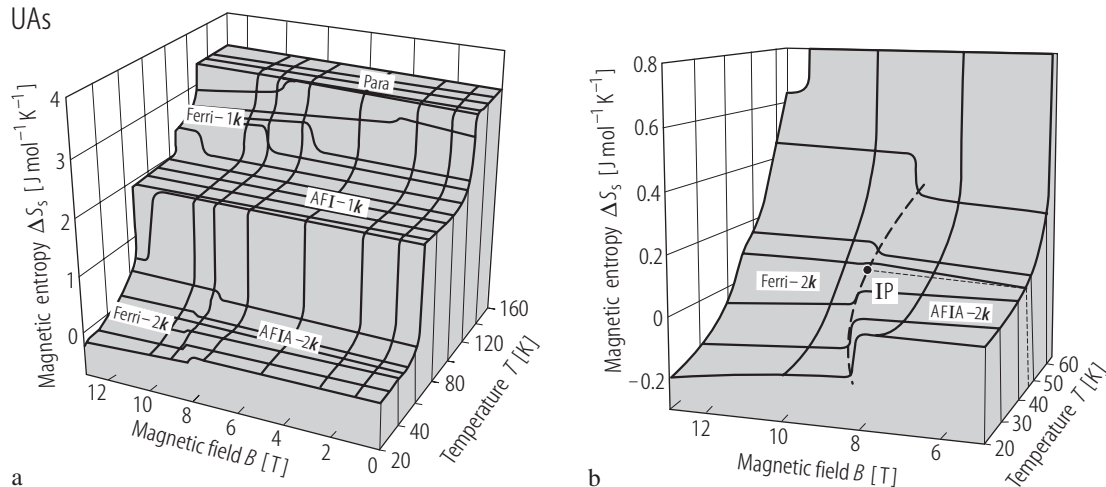


Fig. IV.62. UAs s.c. (a) The magnetic entropy difference $\Delta S_s = S_s(T, B) - S_s(20 \text{ K}, 0 \text{ T})$ vs. temperature, T , (20...160 K) and applied magnetic fields B up to 13 T [03PJBS]. (b) A magnification of the above (T, B) dependences of ΔS_s

around the AF IA-2k/ Ferri-2k phase transition line. See the inversion point (IP) at 46.2 K and $B = 9.30 \text{ T}$ (the full circle). The dashed line is the phase border between the above mentioned phases.

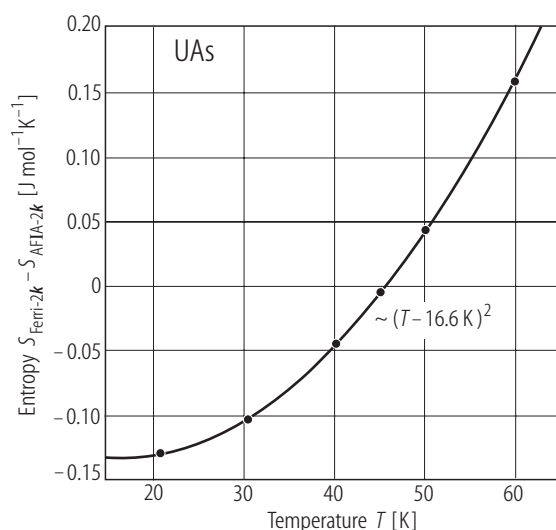


Fig. IV.63. UAs s.c. The entropy jump ΔS on the AF IA-2k/ Ferri-2k phase transition line vs. temperature, T , [03PJBS]. Due to $M_T = 0$ within both regions of existence of the above phases, the jump in ΔS is equal to the difference: $\Delta S = S_{\text{Ferri-2k}} - S_{\text{AF IA-2k}} = \Delta S_{\text{min}} + a(T - T_{\text{min}})^2$, where $\Delta S_{\text{min}} = -0.13 \text{ J/mol K}$, $T_{\text{min}} = 16.6 \text{ K}$ and $a = 1.53 \cdot 10^{-4} \text{ J/mol K}^3$. The small values of ΔS between both phases are only a small part of their total magnetic entropy S_{magn} (see [80BTLM]). This indicates that the above magnetic rearrangement concerns only a subsystem of the whole magnetic structure.

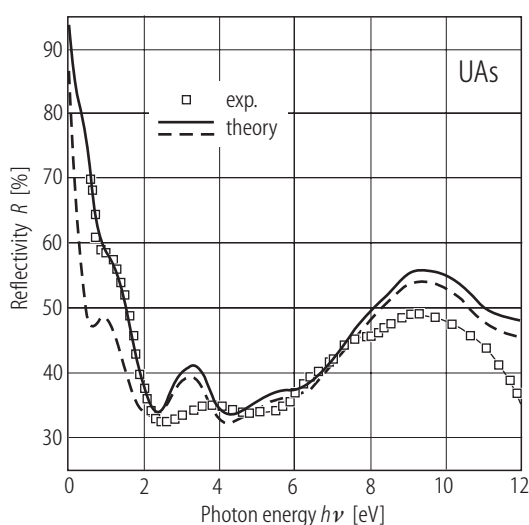


Fig. IV.64. UAs. Calculated and experimental reflectivity spectrum, R , vs. photon energy, $h\nu$, [05KO]. The dashed curve gives the *ab initio* calculated reflectivity without the intraband Drude contribution, while the solid curve gives the *ab initio* calculated reflectivity including a phenomenological Drude term (with $\sigma_D = 4 \cdot 10^{15} \text{ s}^{-1}$, $\delta_D = 0.45 \text{ eV}$). The experimental data (open squares) are from [80S3] and are shown in Fig. IV.65.